frontiers in Earth Science

ORIGINAL RESEARCH
published: 11 June 2021
doi: 10.3389/feart.2021.665185

Geologic and Structural Evolution of the NE Lau Basin, Tonga: Morphotectonic Analysis and Classification of Structures Using Shallow Seismicity

Melissa O. Anderson[1], Chantal Norris-Julseth[1], Kenna Harmony Rubin[2], Karsten Haase[3], Mark D. Hannington[4,5], Alan T. Baxter[4] and Margaret S. Stewart[6]*

[1]Department of Earth Sciences, University of Toronto, Toronto, ON, Canada, [2]Department of Geology and Geophysics, SOEST, University of Hawaii, Honolulu, HI, United States, [3]GeoZentrum Nordbayern, Friedrich-Alexander University of Erlangen-Nürnberg, Erlangen, Germany, [4]Department of Earth Sciences, University of Ottawa, Ottawa, ON, Canada, [5]GEOMAR, Helmholtz Centre for Ocean Research Kiel, Kiel, Germany, [6]Department of Earth and Environmental Sciences, Mount Royal University, Calgary, AB, Canada

OPEN ACCESS

Edited by:
Ziyadin Cakir, Istanbul Technical University, Turkey

Reviewed by:
Jonathan Sleeper, University of Hawaii–West Oahu, United States
Mehmet Korhan Erturac, Sakarya University, Turkey
Martin Patriat, Institut Français de Recherche pour l'Exploitation de la Mer (IFREMER), France

***Correspondence:**
Melissa O. Anderson
melissao.anderson@utoronto.ca

Specialty section:
This article was submitted to Structural Geology and Tectonics, a section of the journal Frontiers in Earth Science

Received: *07 February 2021*
Accepted: *12 May 2021*
Published: *11 June 2021*

Citation:
Anderson MO, Norris-Julseth C, Rubin KH, Haase K, Hannington MD, Baxter AT and Stewart MS (2021) Geologic and Structural Evolution of the NE Lau Basin, Tonga: Morphotectonic Analysis and Classification of Structures Using Shallow Seismicity. Front. Earth Sci. 9:665185. doi: 10.3389/feart.2021.665185

The transition from subduction to transform motion along horizontal terminations of trenches is associated with tearing of the subducting slab and strike-slip tectonics in the overriding plate. One prominent example is the northern Tonga subduction zone, where abundant strike-slip faulting in the NE Lau back-arc basin is associated with transform motion along the northern plate boundary and asymmetric slab rollback. Here, we address the fundamental question: how does this subduction-transform motion influence the structural and magmatic evolution of the back-arc region? To answer this, we undertake the first comprehensive study of the geology and geodynamics of this region through analyses of morphotectonics (remote-predictive geologic mapping) and fault kinematics interpreted from ship-based multibeam bathymetry and Centroid-Moment Tensor data. Our results highlight two notable features of the NE Lau Basin: 1) the occurrence of widely distributed off-axis volcanism, in contrast to typical ridge-centered back-arc volcanism, and 2) fault kinematics dominated by shallow-crustal strike slip-faulting (rather than normal faulting) extending over ~120 km from the transform boundary. The orientations of these strike-slip faults are consistent with reactivation of earlier-formed normal faults in a sinistral megashear zone. Notably, two distinct sets of Riedel megashears are identified, indicating a recent counter-clockwise rotation of part of the stress field in the back-arc region closest to the arc. Importantly, the Riedel structures identified in this study directly control the development of complex volcanic-compositional provinces, which are characterized by variably-oriented spreading centers, off-axis volcanic ridges, extensive lava flows, and point-source rear-arc volcanoes. This study adds to our understanding of the geologic and structural evolution of modern backarc systems, including the association between subduction-transform motions and the siting and style of seafloor volcanism.

Keywords: NE lau basin, back-arc, geologic mapping, submarine volcanism, megashear, morphotectonic analysis, centroid moment tensors

INTRODUCTION

Back-arc basins are extensional features formed behind subduction zones by progressive rifting of volcanic arcs or behind the arc fronts in pre-existing oceanic basins until passive mantle upwelling creates new oceanic crust (Karig, 1970). Their initiation is triggered by processes of either hinge-rollback (Chase, 1978; Scholz and Campos, 1995), and/or upper plate migration away from the trench associated with slab anchoring (Uyeda and Kanamori, 1979; Scholz and Campos, 1995; Heuret and Lallemand, 2005). Migration of the trench relative to the overriding plate leads to a diverse arrangement of plates and deformation styles within the near-arc and back-arc environments (Heuret and Lallemand, 2005). Edge-driven kinematics are common along the boundaries of microplates, where microplate rotation is driven by the motion of the two larger plates the microplate is pinched between (Schouten et al., 1993). These microplate rotations can cause block rotations, shearing, and further rift propagation (e.g., Easter Microplate: Neves et al., 2003). Hinge-rollback, seamount subduction, microplate interactions, and variations in trench geometry and/or subduction angle all influence the state of stress in the overriding plate, driving upper mantle flow and magmatic upwelling, and the formation of structures that provide pathways for magma to reach the surface. However, seismologic data alone cannot fully resolve the types of faulting, and therefore the stress regimes that lead to the emergence of these structures often remain enigmatic.

This paper focuses on the geological and structural evolution of the NE Lau Basin, which is one of the most volcanically- and tectonically-active places on Earth (Embley et al., 2009; Rubin et al., 2013; Embley and Rubin, 2018). New high-resolution multibeam bathymetry collected by the R/V Falkor expedition FK171110 in 2017 and R/V Sonne expedition SO-263 in 2018 are compiled with previously collected bathymetry and are used for morphotectonic analyses. Interpretations of this data, together with seafloor samples and ground truthing, are used to create the first remote-predictive geologic and structural maps of the region. The structures are further classified based on shallow seismicity (Centroid Moment Tensors) to provide insight into the recent kinematic evolution of the faulting. This analysis provides context for understanding the controls on the development of large magmatic-hydrothermal systems across the study area.

TECTONIC SETTING

The Tonga-Kermadec subduction zone in the western Pacific extends over 2,000 km from New Zealand to Fiji, where the Pacific Plate subducts westward beneath the Indo-Australian Plate (**Figure 1**). Collision of the Louisville Seamount Chain with the trench has segmented the subduction zone into the Tonga Trench in the north and the Kermadec Trench in the south. This collision induced compression in the fore-arc and may have influenced where and when rifting in the back-arc occurred (Ruellan et al., 2003). Rifting of the Tonga Arc at 5.5–6 Ma formed the Lau Basin (**Figure 2**), which evolved to mature seafloor spreading along multiple spreading centers at ca. 4 Ma (Zellmer and Taylor, 2001; Taylor and Martinez, 2003). Arc volcanism shifted from the remnant Lau Ridge to form the new Tofua Arc at 3.5 Ma (Tappin et al., 1994). In the southern part of the subduction zone, rifting of the Kermadec Arc at ca. <2 Ma produced the Havre Trough (Wysoczanski et al., 2019).

The orientation of the modern Tonga Trench is north-easterly, with a sharp bend to a westerly direction at the northern apex where there is a transition from subduction to transform motion. This transition is associated with a Subduction-Transform-Edge-Propagator (STEP; Govers and Wortel, 2005). In the following, we refer to the east-west transform boundary as the "STEP fault," which is associated with vertical tearing that causes a piece of the subducting plate to remain at surface (Govers and Wortel, 2005; Nijholt and Govers, 2015). Behind the arc, the modern Lau Basin displays a tapering V-shape with a width of ~500 km in the north, narrowing to 200 km in the south where it merges with the Havre Trough at 26°S (**Figure 2**). In the south of the Lau Basin, two plates (Tonga and Australian) are separated by a single segmented spreading center. The number of spreading centers increases northward, indicating increasing tectonic complexity (Sleeper and Martinez, 2016). The Niuafo'ou Microplate in the north has been interpreted to occur between the Tonga and Australian plates, although it is bounded by and contains numerous small spreading centers and propagating rifts, and so structurally might be even more complex (i.e., multiple microplates). There are likely several other micro- or nano-plates in the northern basin with poorly defined (possibly diffuse) boundaries (Zellmer and Taylor, 2001; Phillips, 2003; Conder and Wiens, 2011; Baxter et al., 2020).

Plate reconstructions by Sleeper and Martinez (2016) suggest that non-rigid plate behavior may be important in this area, where plate boundaries can propagate and rotate, and experience intraplate deformation. Notably, the NE Lau Basin is dominated by strike-slip faulting, revealed by analysis of focal mechanisms of shallow crustal earthquakes (Hawkins, 1995; Baxter et al., 2020). Baxter et al. (2020) describe these focal mechanisms across the entire Lau Basin, and interpret strike-slip faulting to result from re-activation of normal faults produced along spreading centers. In this study, we focus on the structures of the NE Lau Basin in greater detail, complemented by morphotectonic analyses (remote-predictive geologic mapping), in order to better understand the origin and evolution of strike-slip faulting and the possible influence on back-arc magmatic-hydrothermal processes.

DATA AND METHODS

This study combines large hydro-acoustic datasets (multibeam bathymetry and backscatter) and seafloor sampling and observations from the past decade. Interpretation of this data (including morphotectonic analyses) is used to generate a remote-predictive geological map of the study area. This is critical for understanding the controls on the distribution of structural and geologic features. Publicly available Centroid

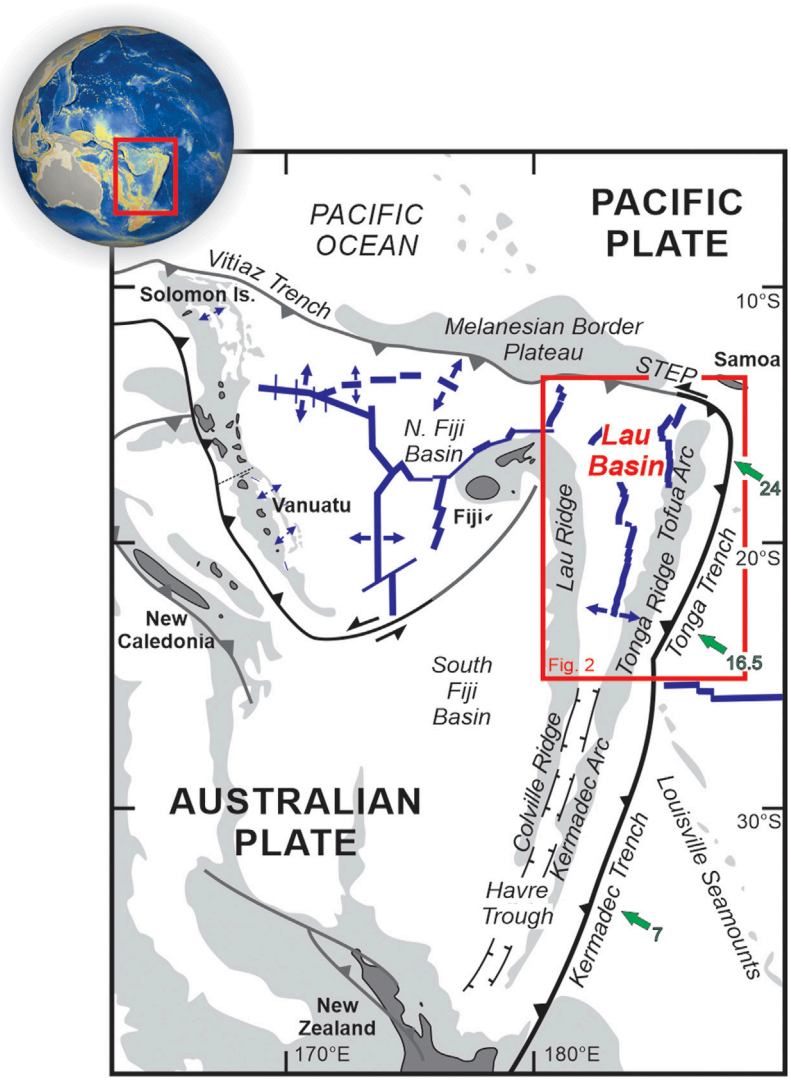

FIGURE 1 | Geographic location and tectonic features of the southwest Pacific modified from Hall (2002). Light gray areas represent the 2,000 m isobaths, green arrows indicate convergence directions and rates (cm/yr) from Bevis et al. (1995), and blue lines represent spreading centers. STEP, subduction-transform-edge-propagator fault.

Moment Tensor (CMT) data is interpreted together with the orientations of nearby structures to investigate fault kinematics.

Bathymetric Data and Remote-Predictive Geologic Mapping

Ship-based multibeam bathymetric data from the NE Lau Basin were collected during 2 R/V Kilo Moana cruises in 2010 (KM1024; Rubin and Shipboard Scientific Party, 2010) and 2011 (KM1129; Martinez and Shipboard Scientific Party, 2013), and are supplemented here with new data from R/V Falkor cruise FK171110 in 2017 (Merle et al., 2018), and R/V Sonne cruise SO-263 in 2018 (Tonga Rift: Haase and Shipboard Scientific Party, 2018). The R/V Kilo Moana and R/V Sonne are equipped with Kongsberg EM 122 multibeam echo sounders with operating frequencies of 12 kHz, and the R/V Falkor is equipped with a Kongsberg EM 302 multibeam echo sounder with an operating frequency of 30 kHz. This data is combined with a regional bathymetric compilation of the area by F. Martinez for the NSF-Ridge 2000 (R2K) program (Sleeper and Martinez, 2016). The combined surveyed area is 40,760 km^2, covering 73% of the map area (**Figure 3**, **Supplementary Figure S1**). The raw multi-beam data were cleaned and gridded at cell sizes of 30–50 m by the various shipboard scientific parties. The data were compiled together with the 2019 GEBCO grid (GEBCO Compilation Group, 2019) and reprocessed using the "Terrain Texture Shading" (TTS) technique developed by Brown (2014) as an interpretive tool in applied geomatics to reveal subtle surface and structural features that can be directly correlated with seafloor geomorphology (e.g., Anderson et al., 2016; Augustin et al., 2016; Anderson et al., 2017). Hydroacoustic backscatter data was also collected during the FK171110 cruise (**Supplementary Figure S2**). The intensity of

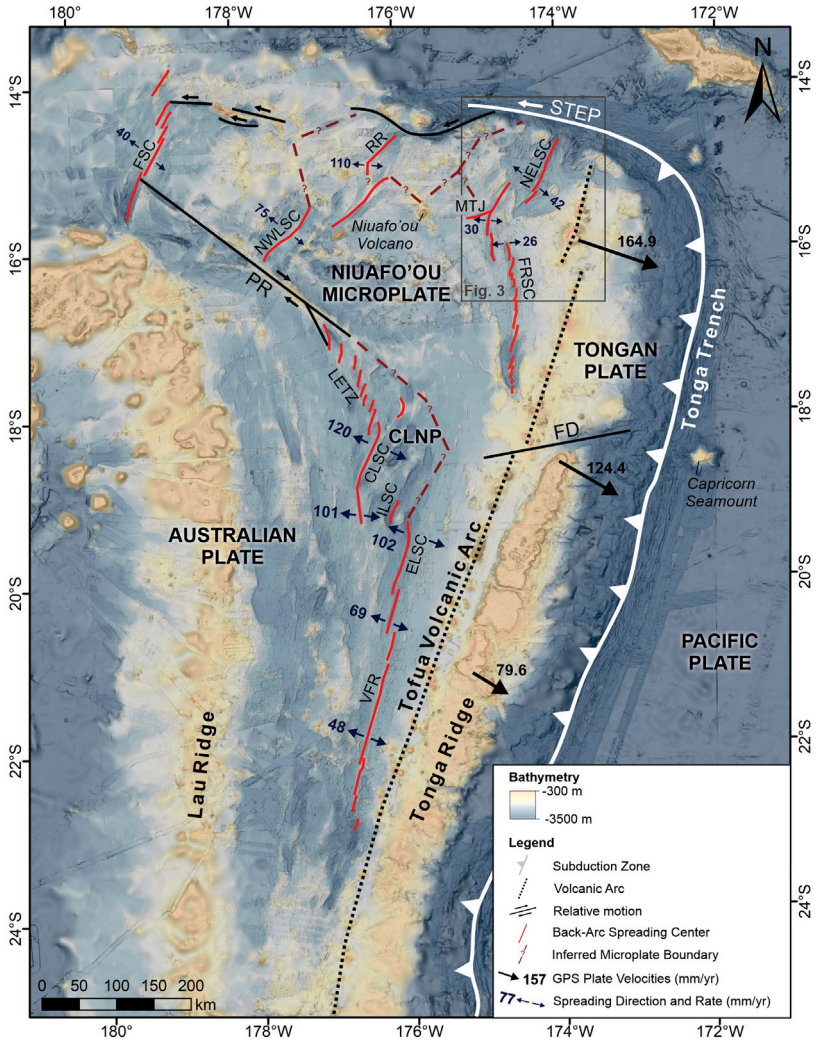

FIGURE 2 | Tectonic features and regional bathymetry of the NE Lau Basin compiled from Rubin and Shipboard Scientific Party (2010), Martinez and Shipboard Scientific Party (2013), Sleeper and Martinez, (2016), Rubin and Shipboard Scientific Party (2018), Haase and Shipboard Scientific Party (2018), and GEBCO Compilation Group (2019). Inferred microplate boundaries based on seismicity from Conder and Wiens (2011), GPS velocities of Tonga relative to Australia from Phillips (2003) and spreading directions and rates (mm/yr) for the FSC from Pelletier et al. (2001), for the NWLSC and RR from Lupton et al. (2015) following Bird (2003), and for the CLSC, ELSC, FRSC, LETZ, MTJ, NELSC, and VFR from Sleeper and Martinez (2016). CLNP, central lau nano-plate; CLSC, central lau spreading center; ELSC, eastern lau spreading center; FD, fonualei discontinuity; FRSC, fonualei rift and spreading center; FSC, futuna spreading center; ILSC, intermediate lau spreading center; LETZ, lau extensional transform zone; MTJ, mangatolu triple junction; NELSC, north-east lau spreading center; NWSC, north-west lau spreading center; PR, peggy ridge; RR, rochambeau rifts; VFR, valu fa ridge.

the backscatter signal is an important indicator for the nature of the seafloor, where strong signal returns indicate hard substrates (such as young lava flows), whereas signals become attenuated with increasing sediment cover. Variations in the seafloor rugosity and slope also affect the backscatter signal.

The morphology of the seafloor is characterized by several important factors derived from the bathymetry, including slope, rugosity (or vector ruggedness measure), and aspect, which were explored using the Benthic Terrain Modeler (BTM) 3.0 add on in ArcGIS v.10.6 (**Figure 3**). The distribution of these morphologic features was interpreted together with backscatter data to define the classification scheme for a remote-predictive geological map, following the criteria outlined by Anderson et al. (2016), Anderson et al. (2017), and Klischies et al. (2019). Lithologies were then ascribed to these units based on available data from ROV sampling, TV grabs (visually aided ship-based scoop sampling), and wax coring from the FK171121 and SO-263 cruises and a compilation of data from literature (**Supplementary Figure S3**; Falloon et al., 1987; Volpe et al., 1988; Loock et al., 1990; Sunkel, 1990; Falloon and Crawford, 1991; Falloon et al., 1992; Poreda and Craig, 1992; Danyushevsky et al., 1993; Hilton et al., 1993; Honda et al., 1993; Dril et al., 1997; Ewart et al., 1998; Sun et al., 2003; Turner et al., 2006; Falloon et al., 2007; Keller et al., 2008; Layne et al., 2009; Lupton et al., 2009; Tian et al., 2011; Dale et al., 2012; Hahm et al., 2012; Lupton et al., 2012; Lytle et al., 2012; Meffre et al., 2012; Birner et al., 2017;

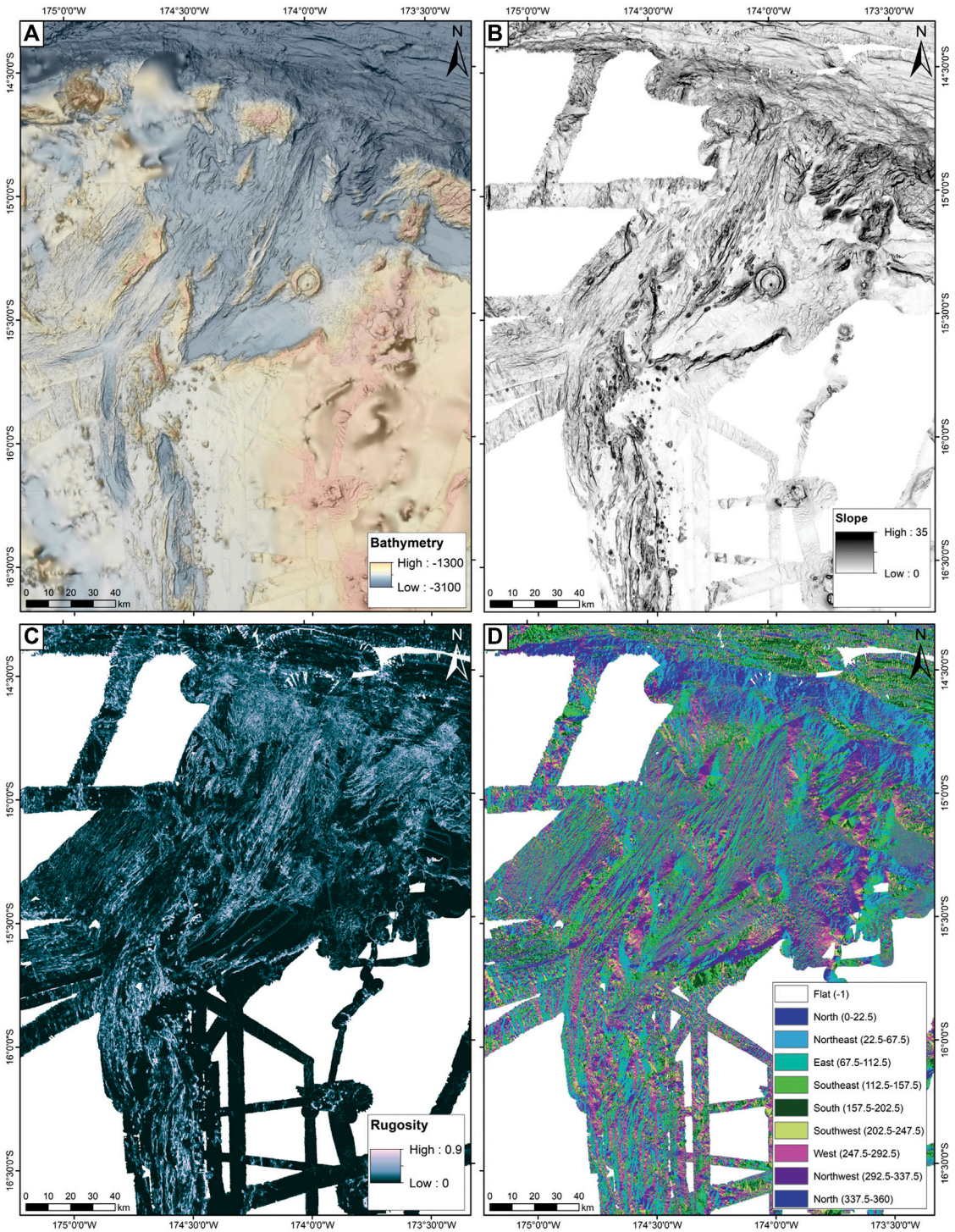

FIGURE 3 | Ship multibeam bathymetry and derived datasets from the NE Lau Basin: **(A)** ship multibeam bathymetry from Rubin and Shipboard Scientific Party (2010), Martinez and Shipboard Scientific Party (2013), Sleeper and Martinez, (2016), Merle et al. (2018), and Haase and Shipboard Scientific Party (2018), overlain on the GEBCO 2019 regional bathymetric grid (GEBCO Compilation Group, 2019), processed using Terrain Texture Shading (after Brown, 2014); **(B)** slope of the ship multibeam bathymetry compilation; **(C)** rugosity (or vector ruggedness measure) of the ship multibeam bathymetry compilation; and **(D)** aspect of the ship multibeam bathymetry compilation.

Nielsen et al., 2017; Brens et al., 2018; Embley and Rubin, 2018; Kendrick et al., 2019; Wang et al., 2019; Zhu et al., 2020). In addition to these morphological/lithological units, fully georeferenced measurements of structural features, including faults with visible throws, volcanic ridges with symmetrical profiles, and lineaments are manually interpreted and digitized at a scale of 1:100,000, following the procedure outlined by Anderson et al. (2017). Lineaments are further classified according to orientation, and relative lineament densities (lineament km per km^2) for each lineament orientation are determined using the "Line Density Tool" in ArcGIS v.10.6 (Spatial Analyst add-on). Relative ages of the mapped units were established from overlapping, embayment, and cross-cutting relationships (e.g., if one lava flow onlaps another, or one structure displaces another), and morphological and backscatter evidence of young volcanic flow features and sediment cover.

Further "ground-truthing" of the map legend was provided by seafloor observations during ROV dives; seventeen dives were performed with the MARUM ROV Quest 4000 during the 2018 SO-263 cruise (Haase and Shipboard Scientific Party, 2018), and seven dives were performed during the TN234 cruise using WHOI ROV Jason-2 (five dives at West Mata and two dives on the southern NELSC; Resing and Shipboard Scientific Party, 2009). The SO-263 QUEST 4000 dives included one that transected the wall of the graben in the NE map area that hosts the Niua volcano (Escarpment A), one that transected the northern Tonga forearc, six dives at vent sites at the Niua arc volcano, six dives at various locations around Niuatahi volcano, and two dives at the southern NELSC near the Maka seamount and its summit hydrothermal vent site (Haase and Shipboard Scientific Party, 2018).

Shallow Seismicity and Fault Kinematics

Seismic data was collected from the Global Centroid Moment Tensor (GCMT) project (www.globalcmt.org; accessed September 2018) over the study area, filtering for shallow (≤25 km) earthquakes limited to the upper plate and excluding CMTs that may be associated with the down-going slab. All CMTs included in the dataset ($n = 174$) are large magnitude with Mw > 5.0, and includes values for the strike, dip, and rake of two possible focal planes. To determine the correct focal plane solution, each CMT was interpreted in the context of the dominant lineament orientation (e.g., **Supplementary Figure S3**), plotted using the ArcBeachball tool (v.2.2). This technique has been used since scientists first started recording seismic moments (e.g., McKenzie, 1969) and is described in detail by Baxter et al. (2020). This data was used for interpretation of fault kinematics and is supplemented by interpretations of offset features where cross-cutting relationships exist.

RESULTS: GEOLOGICAL AND STRUCTURAL FEATURES OF THE NE LAU BASIN

Most of the prior work toward understanding the geology of the Lau Basin has been on regional-scale studies of the crustal evolution and shallow seismicity (e.g., Sleeper and Martinez, 2016; Baxter et al., 2020; Stewart et al., in press). Higher-resolution studies have focused on the southern basin along the Eastern and Central Lau Spreading Centers, where crustal accretion resembles mid-ocean ridges. This contrasts the processes of crustal accretion in the NE Lau Basin, where a diffuse system of back-arc extension, short-lived rifts, spreading centers, jumping ridge crests, and point-source volcanism dominate (Taylor et al., 1996; Embley et al., 2009). In the study area, there are five distinct crustal types: Lau back-arc crust, Lau rear-arc crust, Tofua arc crust, paleo-arc crust, and Pacific Plate crust (undifferentiated), as shown in **Figure 4** and described in **Supplementary Table S1**. These crustal types are primarily based on lithological information (**Supplementary Figure S3**), relative locations, inferred ages from literature data, and seafloor morphology. Additional constraints are provided by vertical gravity gradient (VGG) anomalies from the CryoSat-2 and Jason-1 missions (Sandwell et al., 2014), and seafloor magnetization anomalies (0.5-arc-minute: Austin, 2012, and references therein). These data highlights areas of focused crustal accretion such as back-arc spreading centers or volcanoes, which appear as gravity highs in the VGG data and tend to correlate with positive magnetic anomalies. Finally, we also extrapolate multichannel seismic reflection data along the FRSC (Schmid et al., 2020) to distinguish the approximate transition from arc crust to back-arc crust.

Based on detailed morphotectonic analyses and additional ground-truthing data, we present new remote-predictive geological and structural maps of the NE Lau Basin at high-resolution (**Figures 5–7**; **Supplementary Table S2**), which highlight the wide variety of rock types, extensive volcanism, and complex structural fabrics resulting from the dynamic evolution of the area. We categorize our map into nine assemblages, which are characterized by distinct modes of formation (e.g., related to specific spreading centers or volcanic/sedimentary processes) and geochemical signatures. Each assemblage contains one or more physiographic units, which display internal uniformity in terms of seafloor morphology (e.g., smooth vs. hummocky) and interpreted mode of formation (e.g., lava flow vs. sediment), as well as relative age when determinable (e.g., through embayment relationships, acoustic backscatter signature).

Lau Back-Arc Crust: Rifts and Spreading Centers

The spreading centers in the study area include the three arms of the Mangatolou Triple Junction (MTJ; formerly the "Kings Triple Junction"), the North-East Lau Spreading Center (NELSC), and the northern half of the Fonualei Rift and Spreading Center (FRSC). The spreading centers primarily erupt basalt, with lesser amounts of basaltic andesite, andesite, rhyolite, and boninite, with distinct geochemical signatures along each spreading center (Falloon et al., 2007; Tian et al., 2011; Escrig et al., 2012; Haase and Shipboard Scientific Party, 2018; Rubin and Shipboard Scientific Party, 2018). Sampling of the MTJ has revealed a diverse suite of lithologies, spanning the compositional range from basalt to andesite to dacite (Nilsson et al., 1989; Falloon et al., 1992; Hawkins, 1995; Langmuir et al., 2006). The NELSC

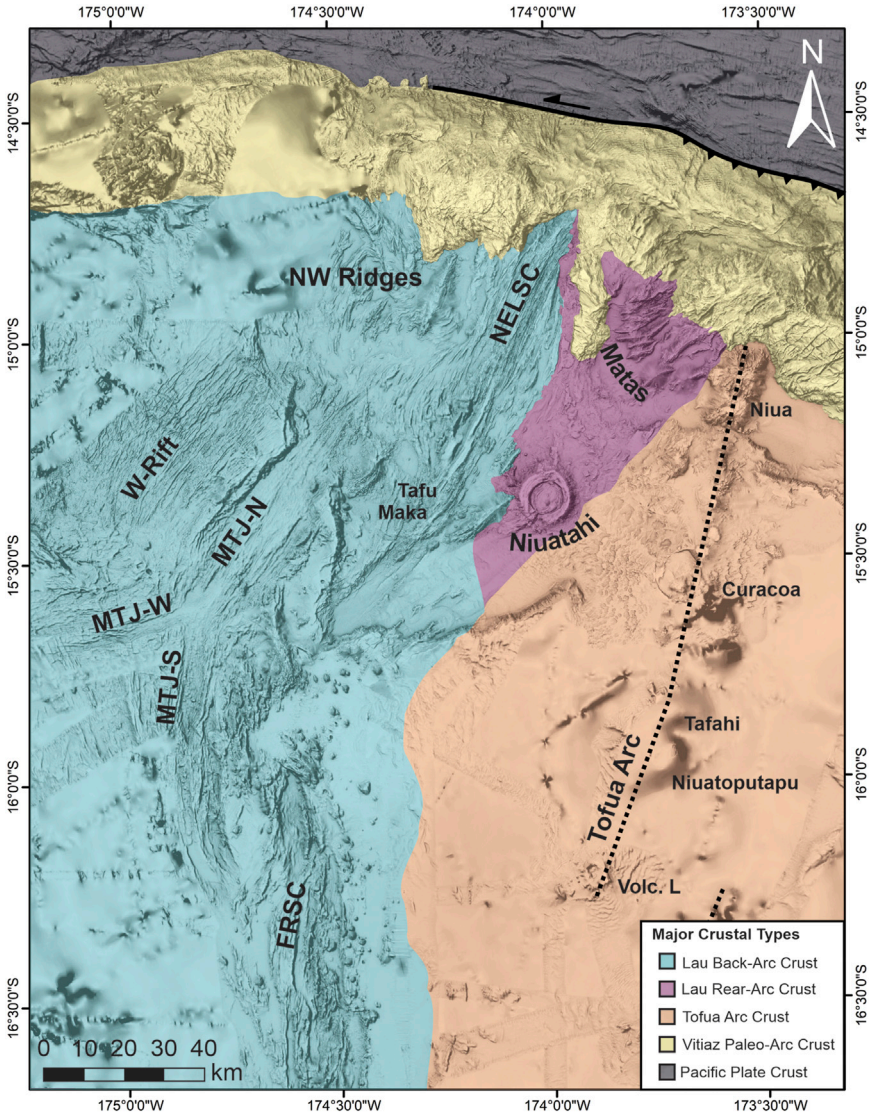

FIGURE 4 | Crustal types in the study area overlain on a compilation of ship multibeam bathymetry (compilation data as in **Figure 3**), described in detail in **Supplementary Table S1**. Note that the contacts between crustal types are approximate. "Matas" refers to the Mata volcanos; other abbreviations as in **Figure 2**.

has a mixed geochemical signature of OIB and N-MORB, in addition to subtle arc-like affinities (Keller et al., 2008; Zhang et al., 2018). Along the southern MTJ arm and the FRSC, IAB signatures are most abundant, with boninitic signatures in the central FRSC associated with magmas captured from the volcanic front (Escrig et al., 2012). Despite the proximity of these spreading centers (~30 km), there is a distinct compositional change between them (e.g., Keller et al., 2008). Therefore, these spreading centers are mapped as separate geological assemblages, each consisting of several units (**Figure 5**).

Mangatolou Triple Junction and Western Rift Zone Assemblages

The MTJ is a ridge-ridge-ridge triple junction with each of the three spreading segments displaying distinct morphologies (**Figure 5**). The MTJ assemblage consists of a neovolcanic zone along the center of each segment, flanked by older crust that is variably faulted or ridge-like. The western arm (MTJ-W) is oriented ENE, accommodating N-S extension in the basin, and is considered to be a failed rift (Phillips, 2003). This arm has a narrow neovolcanic zone (up to 3 km wide) within a flat axial valley and is heavily faulted, with structures that are oriented ENE to E-W (**Figures 7D,E**). The southern arm (MTJ-S) consists of two spreading segments that are oriented N-S, with an axial valley containing a neovolcanic zone that is up to 5 km wide. This neovolcanic zone is dominated by sheet flows and small fissures. Distal volcanic ridges along the flanks of the MTJ-S extend up to 40 km to the west of the spreading center and are steeper and have more relief than ridges along the other arms. In the northern part of the MTJ-S arm, the ridges are cross-cut by E-W trending faults

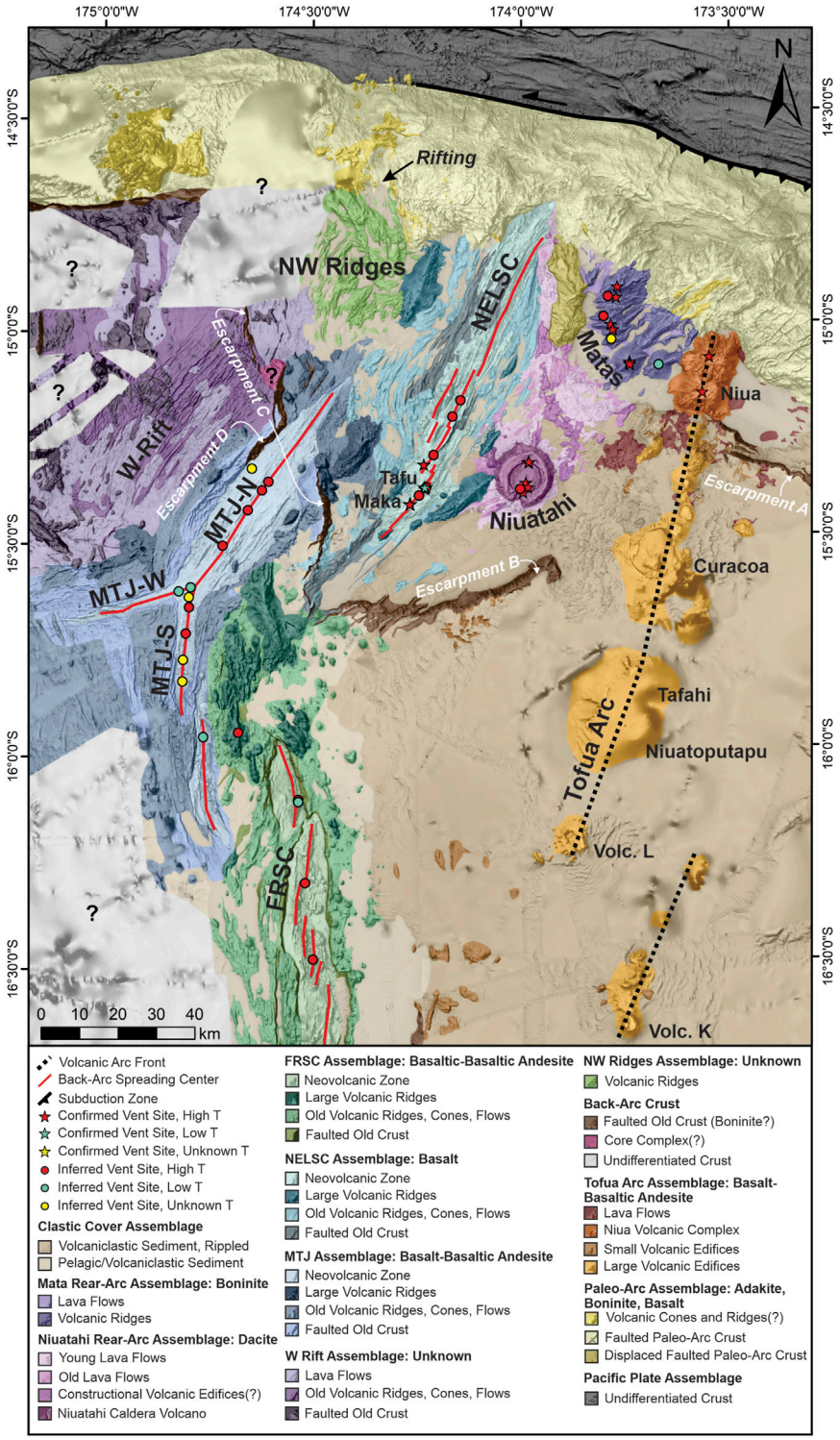

FIGURE 5 | Remote-predicted geological map of the NE Lau basin interpreted from seafloor geomorphology and limited sampling (**Supplementary Figure S3**), overlain on a compilation of ship multibeam bathymetry (compilation data as in **Figure 3**). Hydrothermal vent sites compiled from the FK171111 and SO-263 cruises (Haase and Shipboard Scientific Party, 2018; Rubin and Shipboard Scientific Party, 2018), InterRidge Vents Database v. 3.4 (Beaulieu and Szafranski, 2019), and Baker et al. (2019). "Matas" refers to the Mata volcanoes; other abbreviations as in **Figure 2**. Additional details on map units outlined in **Supplementary Table S2**, lithologies based on sampling shown in **Supplementary Figure S3**.

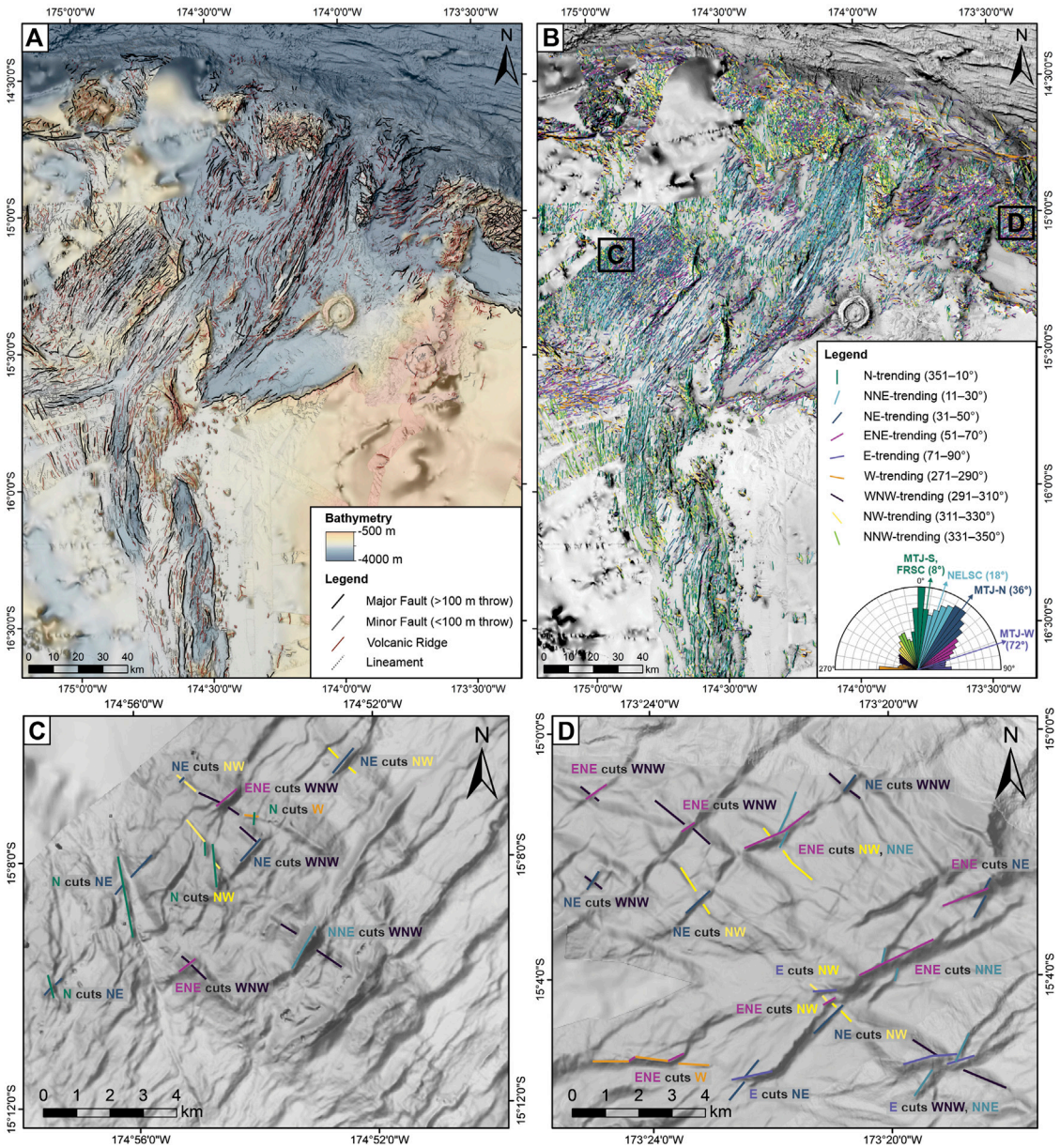

FIGURE 6 | Manually interpreted structural lineaments (mapped at a resolution of 1:100,000) in the NE Lau basin overlain on a compilation of ship multibeam bathymetry (compilation data as in **Figure 3**): **(A)** by type, and **(B)** by orientation. Examples of cross-cutting relationships of selected structures are shown in close-ups for **(C)** the NW rift zone, and **(D)** the paleo-arc crust, summarized in **Table 1**. Higher-resolution maps are provided in **Supplementary Figures S6–S31**.

associated with the MTJ-W arm. The southern part of the MTJ-S arm is dominated by N-trending structures (**Figure 7A**) with minor NNW-trending structures in the south (**Figure 7I**). The northern MTJ arm (MTJ-N) is a single NNE- to NE-trending segment with a broad axial valley up to 18 km wide, which contains the neovolcanic zone and is bounded by steep faults. The northern and southern ends of the segment consist of small volcanic ridges up to ~180 m tall. The central part of the segment has higher relief with a broad shield-like morphology, and a subtle axial graben up to ~2 km wide. Intense off-axis volcanism occurs along a large ridge in the north (centered at 15°18′S, 174°25′W), which is up to 1,300 m tall and 17.5 km long, and an area with large, low-relief cratered volcanoes to the NW of the triple junction (centered at 15°30′S, 174°57′W).

To the west of the MTJ-N arm is an area of rifting with inward-dipping faults and no associated neovolcanic zone, which we refer to as the Western Rift assemblage (**Figure 5**). In the northern part of this assemblage (near Escarpment C in **Figure 5**), the crust is heavily faulted with overlapping zig-zag structures that trend NNE, NE, and ENE (**Figures 7B–D**). In the southern part of this assemblage (nearer to the triple junction in **Figure 5**), the crust is dominated by younger volcanic flows with morphologies

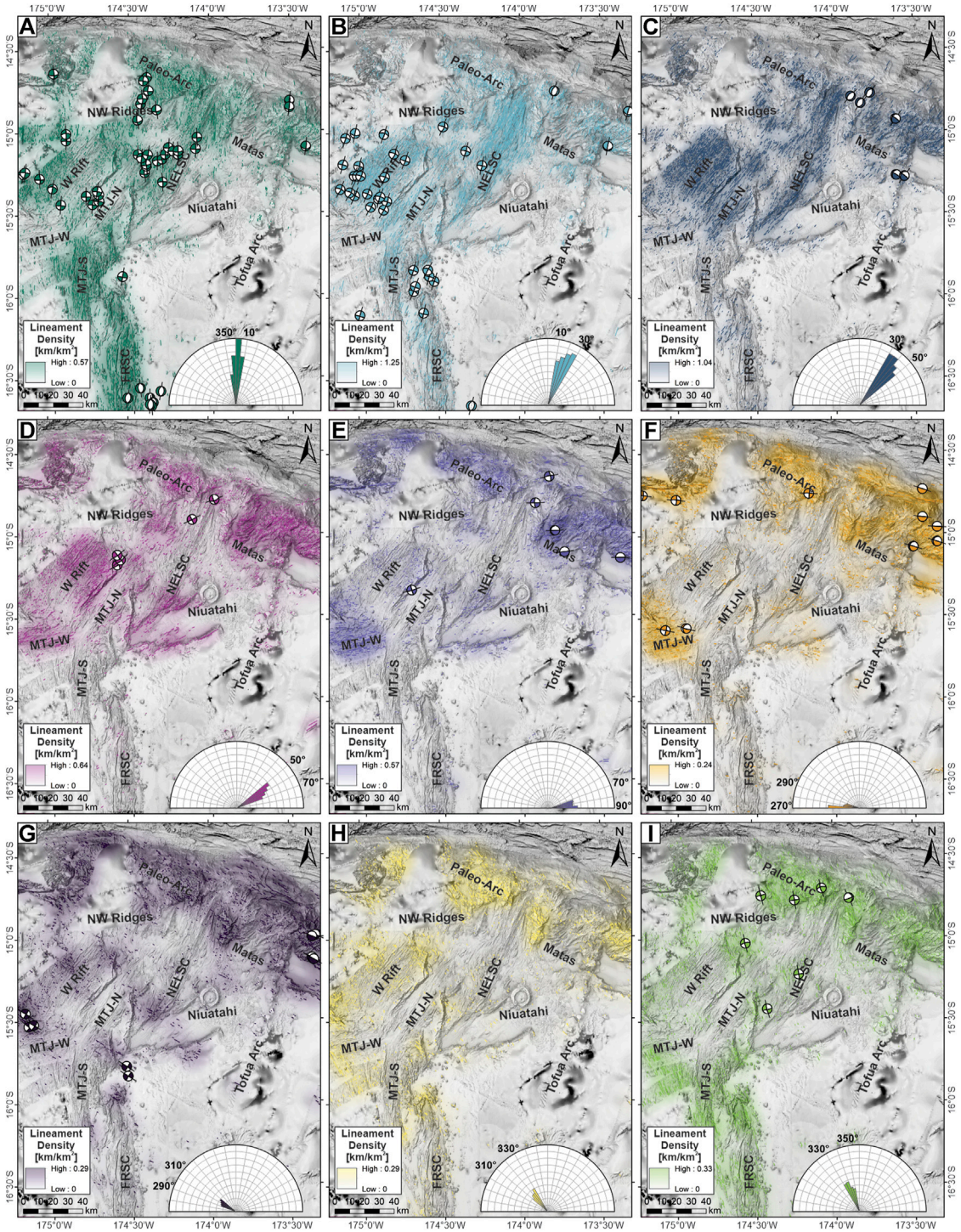

FIGURE 7 | Interpreted structural lineaments, with color shading representing relative lineament densities (lineament km per km^2), and shallow (≤25 km) CMT focal mechanisms from Harvard (www.globalcmt.org; Dziewonski et al., 1981; Ekström et al., 2012), classified according to interpreted focal plane solution: **(A)** N-trending (max. 0.57 km/km^2), **(B)** NNE-trending (max. 1.25 km/km^2), **(C)** NE-trending (max. 1.04 km/km^2), **(D)** ENE-trending (max. 0.64 km/km^2), **(E)** E-trending (max. 0.57 km/km^2), **(F)** W-trending (max. 0.24 km/km^2), **(G)** WNW-trending (max. 0.29 km/km^2), **(H)** NW-trending (max. 0.29 km/km^2), **(I)** NNW-trending (max. 0.33 km/km^2). Stereonets of CMTs grouped according to interpreted focal plane solution are shown in **Supplementary Figure S4**, and close-ups of each of the maps are shown in **Supplementary Figures S32–S40**. Abbreviations as in **Figure 2**, bathymetric compilation as in **Figure 3**.

characteristic of sheet flows with collapse features and lesser amounts of pillow flows. Volcanic flows become more common to the west toward the subaerial Niuafo'ou volcanic island, located outside the study area (**Figure 2**). Cross-cutting the dominant NE-fabric of this area are WNW- and NW-trending volcanic ridges and faults (**Figures 7G,H**). The area has not been previously described or sampled, and therefore the lithology is unknown.

Northeast Lau Spreading Center Assemblage

The NELSC assemblage follows a NE-oriented spreading center that consists of four segments and displays a gently sigmoidal shape (**Figure 5**). The northernmost segment is characterized by a 40 km long axial valley resembling a slow-spreading MOR morphology, while the remaining segments in the south are characterized by axial ridges that are ~15 km in length resembling fast-spreading MOR morphologies. The neovolcanic zone is irregular, between 3.4 and 9.7 km wide. The neovolcanic zone of the northernmost segment consists of elongate hummocky lava flows and mounds. There is a gradual progression southward toward a more flat-topped axial volcanic ridge morphology with point-source volcanic cones. Flat-topped volcanic cones occur near the ends of the NELSC. The southernmost segment is the most magmatically-robust, with axial volcanic ridge highs reaching ~1,260 m above the surrounding seafloor, with large volcanic cones on each termination of the ridge (Maka and Tafu). Proximal to the neovolcanic zone is older, faulted crust, followed by distal heavily-sedimented ridges. These ridges are symmetrical, indicating a volcanic rather than structural origin. Several large volcanic ridges up to 1,570 m tall and 24 km long occur distal to the spreading center, notably to the east of the southern NELSC (centered at 15°24′S, 174°08′W) and to the west of the northern NELSC (centered at 14°55′S, 174°15′W). The structures along this spreading segment are dominantly NNE- and NE-trending (**Figures 7B,C**), with distal N-trending structures associated with volcanic ridges on the SW and NE sides of the spreading center (**Figure 7A**).

Fonualei Rift and Spreading Center Assemblage

The FRSC overlaps with the MTJ-S and is oriented N-S to accommodate E-W extension between the Niuafo'ou and Tonga microplates (**Figure 5**; Sleeper and Martinez, 2016). The FRSC consists of at least six overlapping, left-stepping segments that become progressively closer to the arc toward the south, described by Sleeper et al. (2016). The study area includes the three northern segments, which are ~12–27 km long and are characterized by axial valleys containing a neovolcanic zone up to ~15 km wide. Narrow axial volcanic ridges are surrounded by smooth, featureless seafloor that may be sheet flows or volcaniclastic sediment derived from the nearby volcanic arc. The axial valleys are bounded by steep-sided faults, but unlike other spreading segments in the study area, off-axis faulting is not laterally continuous. The valley flanks are dominated by irregular volcanic ridges and numerous small volcanic cones. To the south of the map area, the axial valleys become less pronounced and there is a transition toward axial ridge morphologies. Based on the width of this assemblage (20–30 km) and the inferred spreading rate (26 mm yr^{-1}; Sleeper and Martinez, 2016) at the northern extent of the FRSC, rifting began between 0.8 and 1.1 Ma. In the north there is an area of robust volcanic activity characterized by coalescing volcanic cones and ridges, as well as a large volcanic ridge, 29 km-long and 1,350 m-tall, extending toward the MTJ-N (centered at 15°41′S, 174°38′W). The transition between the FRSC and the MTJ-N is difficult to distinguish. The structures along the FRSC are dominantly N-trending (**Figure 7A**), with minor NNE- and NNW-trending structures at the northern termination (**Figures 7B,I**).

NW Ridges Assemblage

Finally, an enigmatic area consisting of variably oriented volcanic ridges that are not clearly associated with a spreading center occur in the NW part of the map area, referred to here as the NW Ridges Assemblage (**Figure 5**). Most of the ridges are sub-parallel and oriented NNE to NE (**Figures 7B,C**), with a major ridge trending WNW to NNW (**Figures 7H,I**) rising to a height of 760 m. This major ridge may be an anticline. The areas between the ridges are interpreted to be sediment, although backscatter data is lacking in this area and young lava flows may be present. In the north, the ridges are cut by a N-trending rift (i.e., extensional area with inward-dipping normal faults) that extends into the paleo-arc (described in *Vitiaz Paleo-Arc Crust* below) and appears to be heavily sedimented (labeled "Rifting" in **Figure 5**). The origin of this rift remains enigmatic. The southern contact between this unit and the NW Rift assemblage is poorly defined due to a lack of high-resolution multibeam and backscatter data and may be gradational. The lithology of this assemblage is unknown because it has not yet been sampled.

Lau Rear-Arc Crust

Volcanism that occurs in the back-arc near active arc front but not associated with a spreading center is referred to as rear-arc volcanism, following Embley and Rubin (2018). This is associated with more siliceous lithologies than the back-arc (**Supplementary Figure S3**). In this region, rear-arc volcanism consists of the Mata volcanoes and the Niuatahi volcano and related lava flows and other volcanic features (**Figure 5**). The Mata volcanoes are dominantly boninitic in composition (Resing et al., 2011a), while the Niuatahi volcano and nearby lava flows are dacitic in composition (Embley and Rubin, 2018).

Mata Assemblage

The Mata volcano assemblage occurs in the NE part of the study and consists of nine elongate en echelon volcanic ridges composed of boninitic pyroclastic material and lava flows, surrounded by lava flows (**Figure 5**; Resing et al., 2011a; Rubin and Embley, 2012). These volcanoes have been actively erupting over the last 2 Ma, with older occurrences extending into the fore-arc region (Falloon et al., 2007; Rubin and Embley, 2016; Chadwick et al., 2019). The southern volcanoes, West and East Mata, are 1,400–1,700 m tall and are elongate along an ENE-trend (**Figure 7D**). The West Mata volcano is one of only two places in the world where deep-sea submarine eruptions have been witnessed (Resing et al., 2011b). The Mata volcanoes to the

north (Taha, Ua, Tolu, Fa, Nima, Ono, Fitu) are smaller (900–1,300 m tall) and are variably elongate in ENE- and E-directions.

Niuatahi Assemblage

South of the Mata volcanoes is the Niuatahi assemblage, characterized by the 15 km wide Niuatahi dacite volcano (formerly "Volcano O"), that rises ~1,340 m above the surrounding seafloor with a 9 km-wide nested caldera (**Figure 5**). This volcano is cross-cut by a regional N-trending structure (**Figure 7A**), with E-W extension indicated by short gaps in the caldera walls in the north and south (Baker et al., 2019). Along this regional structure in the south-central part of the caldera is a 465 m-tall resurgent volcanic cone called Motutahi, which is associated with dacite flows (Park et al., 2015) and active venting (Kim et al., 2009). Niuatahi is surrounded by dacite lava flows that extend ~60 km north and northeastward over an area of ~640 km^2, described by Embley and Rubin (2018). Backscatter signatures indicate at least two ages of flows, with the most recent flows displaying a very high backscatter signal (**Supplemental Figure S2**). These dacite flows surround irregularly shaped topographic features, which we interpret to be older constructional volcanic features that represent a central fissure system from which the flows originate.

Tofua Arc Crust

In the study area, the active Tofua arc trends ~18–23° in the south and ~5–8° in the north (**Figure 5**). The Tofua arc assemblage consists of four units: large arc volcanos that consist of a simple conical volcanic edifice (including Volcano L, Volcano K, Niuatoputapu, Tafahi, Curacoa, and other unnamed volcanoes), the Niua volcanic complex that is characterized by an irregular morphology, smaller volcanic edifices that occur on the periphery of the larger edifices, and lava flows. The northern portion of the arc has not been sampled extensively; however, samples collected during the SO-263 cruise ranged from trachyandesite to basalt (Haase and Shipboard Scientific Party, 2018). This is consistent with sampling along the arc adjacent to the FRSC, which is dominantly basaltic andesite (Keller et al., 2008). The Tofua arc volcanoes are dominantly conical submarine stratovolcanoes that decrease in size northwards toward the termination of the arc. Many of these volcanoes have large interior caldera structures. Inactive volcanoes include the submarine volcanoes K and L, which have no documented eruptions in the literature (e.g., seismicity, acoustic response, evidence for recent lava flows), and subaerial volcano Niuatoputapu, which last erupted ~3 My (Global Volcanism Program, 2013). No historical eruptions have been reported at subaerial Tafahi volcano, but the youthful morphology suggests recent (Holocene) activity (Taylor and Ewart, 1997). A recent eruption at the submarine Curacoa volcano was reported in December 1979 (Global Volcanism Program, 2013). At the northern termination of the arc, the submarine Niua volcanic complex (formerly "Volcano P") has a distinct morphology consisting of numerous overlapping cones and ridges and a strongly tectonized appearance (Moum, 2020). This large complex appears roughly rectangular in plan view, up to 25 km long and 13 km wide, and rises to depths of ~2,000 m above the surrounding seafloor. Small (≤100 m tall), dome-like topographic features that are irregularly distributed at the top of the Niua complex are interpreted to be small volcanic edifices. Profuse venting of S-rich magmatic fluids at the Niua North vent site indicate that it is volcanically active (Haase and Shipboard Scientific Party, 2018; Rubin and Shipboard Scientific Party, 2018). Niua is the only place along the Tofua arc in the map area that has confirmed hydrothermal venting (Niua South vent field; Aruculus and Shipboard Scientific Party, 2004). Surrounding the northernmost Niua arc volcano and extending southward toward Curacoa are young lava flows that are identified by high backscatter signatures. We interpret these flows to be genetically related to the Tofua arc volcanoes based on proximity; however, these flows have not been sampled so this relationship is unconfirmed.

Vitiaz Paleo-Arc Crust

The Vitiaz paleo-arc crust occurs in the northernmost part of the map area along the STEP fault and is characterized by a bulging morphology that is heavily tectonized (**Figure 5**). This forms the Paleo-Arc assemblage, which includes the Vitiaz paleo-fore-arc as the morphology does not allow easy distinction. Few samples from this area have been collected, mainly consisting of adakite and boninite (Falloon et al., 2007; Price et al., 2016). The dominant unit in this assemblage consists of faulted old paleo-arc crust, which contains a high density of structures and includes structures of every orientation (**Figure 7**). The youngest unit in this assemblage consists of volcanic cones and ridges that are located at the crest of the bulging morphology of the Vitiaz paleo-arc. These cones and ridges contrast with the intensely faulted appearance of the surrounding paleo-arc crust and therefore appear to be more youthful. These features form in areas adjacent to active back-arc volcanism and therefore may be capturing magmatism from the back-arc or represent extensions of the backarc crust into the paleo-arc terrane. This uncertainty results from a lack of backscatter data and samples in these areas. Finally, an area of intensely faulted terrane to the west of the Mata volcanoes is interpreted to be a unit of detached paleo-arc crust. The structural fabric of this block is dominated by WNW-, NW- and NNW-trending fabrics, similar to the paleo-arc crust on the opposite side of the NELSC (**Figures 7G–I**), and distinct from adjacent assemblages. However, these structural orientations may have been modified during opening of the NELSC, and so the origin remains uncertain. This displaced unit does not show evidence of recent volcanism.

Clastic Cover Assemblage

Clastic sediments are ubiquitous throughout the basin (**Figure 5**), forming a cover sequence on top of the basement crust. This assemblage is divided into two units based on morphology: a rippled volcaniclastic sediment apron that extends from the volcanic arc (e.g., rippled morphology visible in **Supplementary Figure S30**), and a smooth

TABLE 1 | Cross-cutting relationships of structures according to orientation and interpreted Riedel system association, with examples shown in **Figures 6C,D**.

Structure by orientation	Riedel system	Cross-cuts	Cross-cut by	Shear sense
NNE-trending	System 1 R′-shear	System 1 P-shear	System 1 R-shear, System 2 R-shear	R-lateral
E-trending	System 1 R-shear	System 1 R′-shear, System 1 P-shear	None	L-lateral
WNW-trending	System 1 P-shear	None	System 1 R′-shear, System R-shear, System 2 R′-shear	Unknown
N-trending	System 2 R′-shear	System 1 P-shear, System 2 P-shear	System 2 P-shear	R-lateral
ENE-trending	System 2 R-shear	System 1 R′-shear, System 1 P-shear, System 2 P-shear	None	L-lateral
W-trending	System 2 P-shear	System 2 R′-shear	System 2 R′-shear, System 2 R-shear	L-lateral

featureless plain that is likely a combination of pelagic and volcaniclastic sediment. The contact between these two units is gradational, and the contacts with other units tends to be sharp and can be distinguished by the very low backscatter signature. These units onlap other volcanic units in the map area and are therefore interpreted to be the youngest assemblage in the area.

Structural Features

A total of 5,892 major normal fault segments (>100 m throw), 12,071 minor normal fault segments (<100 m throw), 7,420 volcanic ridge segments, and 10,624 lineament segments were interpreted and digitized from the hydroacoustic data (**Figure 6**; higher resolution maps are available in **Supplementary Figures S6–S31**). The distribution of structures according to orientation is shown in **Figure 7** (larger maps are available in **Supplementary Figures S32–S40**), with dominant orientations trending N (0–10°; n = 2,959) and NE (30–40°; n = 3,033).

Cross-cutting relationships between the structures is evident in areas where there is a measurable offset of one structure (i.e., it is cut by another structure). Cross-cutting relationships are most pronounced in highly tectonized areas, namely, the W Rift zone and the Paleo-Arc crust (**Figure 7**). Cross-cutting relationships between structures with similar orientations (e.g., N- and NNE-trending) were not observed, instead these features tend to form zig-zag faults. In general, the structures that are the oldest are NNW-, NW-, and WNW-trending, as they are cross-cut by structures of many orientations (including N-, NNE-, NE-, and E- trending structures) and in turn do not cross-cut any structures. The youngest structures are N-, W-, and ENE-trending and these structures are cross-cut only by themselves. A summary of relative cross-cutting relationships of the major structures in the map area is outlined in **Table 1**. In addition, the direction of the offset provides information about the shear sense for each structure, with R-lateral offsets of the NNE- and N-trending structures, and L-lateral offsets of the E-, ENE-, and W-trending structures (**Table 1**). Examples of select structures and their cross-cutting relationships is shown in **Figures 6C,D**.

Escarpments

There is a distinct three-tiered down-dropped basin topography across the NE Lau Basin (**Figure 3**). The borders of these tiers are defined by large escarpments with throws of up to 1,500 m, which are some of the most striking features in the basin (**Figures 5**, **7A**). A large escarpment in the NE map area ("Escarpment A" in **Figure 5**) forms the wall of the ~WNW-trending basin that hosts the Mata volcanoes and the Niua arc volcano. This escarpment is ~30 km long in the map area and has a maximum throw of 890 m. The dip of this escarpment is variable across its length, averaging 36° to the NNE. One dredge sample from this escarpment was dated at 2.03 ± 0.11 Ma (K-Ar dating; Falloon et al., 2007), although the timing of formation of this escarpment is difficult to constrain due to its association with recent volcanic flows (**Figure 5**). Another ~62 km-long escarpment with a maximum throw of 1,070 m occurs at the southern termination of the NELSC ("Escarpment B" in **Figure 5**) trending ~ENE toward the arc. The average dip is 24° to the NW. Connected to this escarpment in the south is a ~N trending escarpment ("Escarpment C" in **Figure 5**) that becomes NNE-trending with increasing latitude. This escarpment extends ~37 km before it is interrupted by the MTJ-N at 15°19′S. It continues on the opposite side for another ~38 km. This part of the escarpment appears to be interrupted by a detachment fault at 15°07′S (mapped as a core complex in **Figure 5**), characterized by NNW-trending corrugations, although there is a high degree of uncertainty in the identification of this feature. This escarpment appears to comprise multiple stepping faults in places, but in general it has a maximum throw of 1,095 m, dipping ~24° to the E and NE. It is intersected by an NNW-trending escarpment ("Escarpment D" in **Figure 5**) that forms the western boundary of the MTJ-N. This escarpment has a maximum throw of 1,085 m, decreasing in size southwards toward normally-faulted terrain of the MTJ. Using a cutoff throw of 500 m to define this escarpment, it has a length of ~23 km, and dips of 22° to the SE. These dip angles are likely an underestimate of the true dips due to erosional processes over time, indicated by mass wasting features at the base of some of the escarpments.

RESULTS: SHALLOW STRUCTURES (CMTS) AND FAULT KINEMATICS

A total of 174 shallow CMTs (≤25) km are reported in the centroid moment tensor catalog within the map area. Of these,

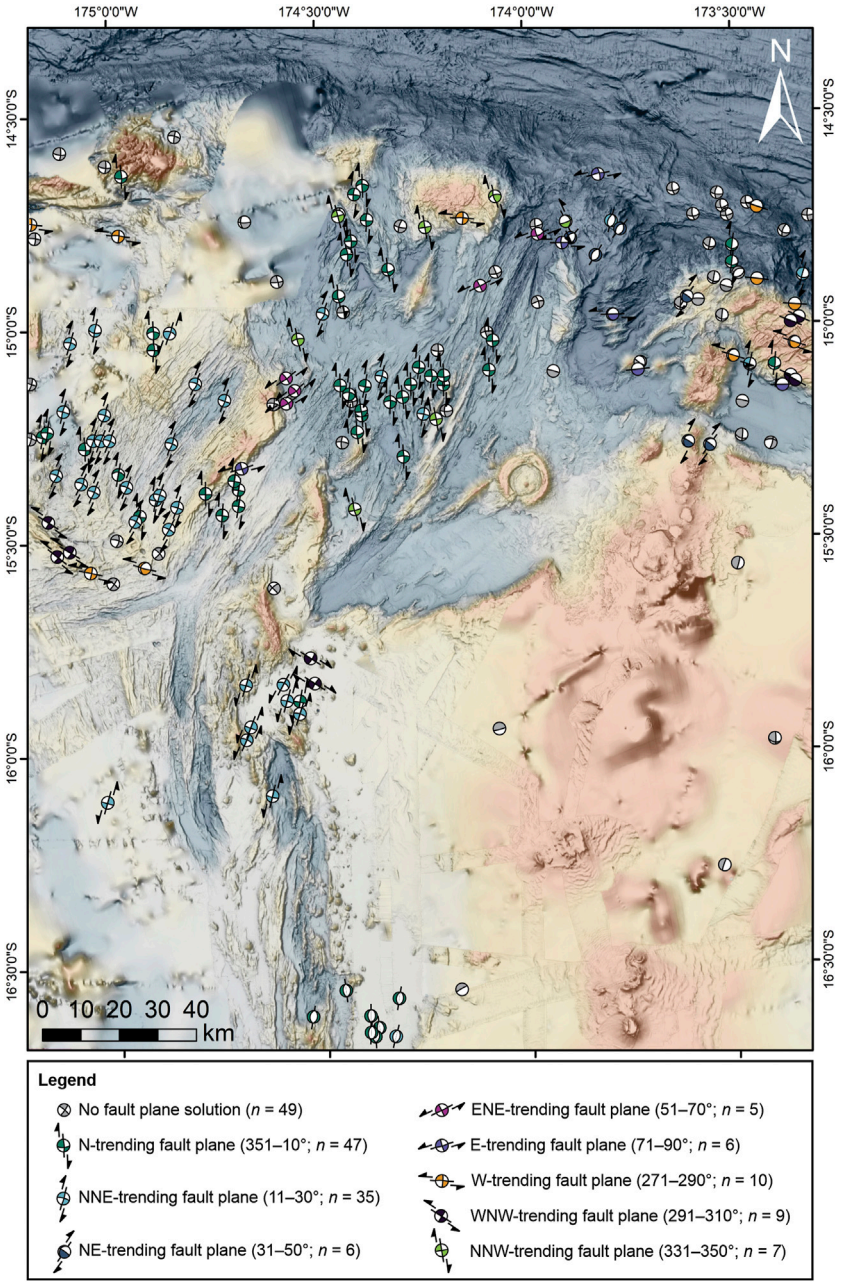

FIGURE 8 | A total of 174 CMTs with shallow depths (≤25 km) occur within the map area (www.globalcmt.org; Dziewonski et al., 1981; Ekström et al., 2012). Of these, 125 CMT focal plane solutions are interpreted by association with the dominant orientation of the seafloor fabric (see **Supplementary Figure S4**). The colors of the CMT "beachball" represent the orientation of the focal plane solution outlined in the legend and shown in detail in **Figure 7**. Bathymetric compilation as in **Figure 3**.

we interpreted the focal planes of 125 CMTs according to their location and proximity to known structural and tectonic features, and classified them according to orientation in **Figures 7**, **8** and **Supplementary Figure S3**. The focal planes of 47 CMTs trend 351–10°, 35 CMTs trend 11–30°, 6 CMTs trend 31–50°, 5 CMTs trend 51–70°, 6 CMTs trend 71–90°, 10 CMTs trend 271–290°, 9 CMTs trend 291–310°, and 7 CMTs trend 331–350°. Fault planes were plotted as stereonets to check for consistency in the groupings (**Supplementary Figure S5**). The fault plane solutions of the remaining 49 CMTs could not be determined (**Figure 8**).

Normal earthquakes comprise only 10% of the CMTs with known focal plane solutions, and these events are restricted to the FRSC in the south of the map area (n = 8; **Figure 7A**), as well as the northern tip of the NELSC (n = 4; **Figures 7B,C**). However, extensional rift-parallel horst-and-graben fault patterns are common across the map area, including within neovolcanic zones and off-axis terrains along the main spreading centers

(**Figure 7A**). Extensional structural fabrics in the NE Lau basin are characterized by two main structural trends. The first trend is parallel to sub-parallel with the NELSC and MTJ-N (NNE- to NE-trending; **Figures 7B,C**). This trend follows the orientation of the Tofua arc between 15°30′S and 17°35′S (southern part of the map area; **Figures 2**, **5**). The second trend is parallel to sub-parallel with the MTJ-S and FRSC (N-trending; **Figure 7A**). This trend follows the orientation of the Tofua arc north of 15°30′S (northern part of the map area; **Figures 2**, **5**). Subordinate structures are orthogonal to these trends but also display normal faulting and extensional features, including the NE- and ENE-trending large volcanic ridges near the southern NELSC and within the Mata volcanic group (**Figures 5**, **7C**,D). The lack of normal faults in the CMT data likely indicate that extension in the basin is simply not producing high-magnitude (Mw > 5) earthquakes. This may indicate that crustal accretion is dominated by magmatic extension with strain accommodated by dike injection rather than tectonic extension with strain accommodated by brittle faulting (e.g., Buck 2004; Buck et al., 2005; Buck, 2006; Ito and Behn, 2008; Wright et al., 2012; Ebinger et al., 2013; Anderson et al., 2017). Alternatively, the lack of CMTs with normal fault plane solutions around the spreading centers may be related to high spreading rates, which are associated with lower magnitude earthquakes (<5 Mw; Macdonald, 1982). Notably, thousands of lower magnitude (<5 Mw) seismic events around the ELSC, CLSC, and FRSC have been recorded by ocean bottom seismometers deployed in these regions (Eguchi et al., 1989; Conder and Wiens, 2011; Schmid et al., 2021), supporting these suggestions.

The CMT data indicate that strike-slip and oblique-slip faulting is widespread across the study area comprising 90% of the interpreted events. This has been described by earlier authors (Hawkins, 1995; Baxter et al., 2020), but here we provide higher-resolution interpretations of the orientation and shear sense interpreted from these CMTs, supported by data of offset features (described in *Shallow Seismicity and Fault Kinematics*). The main N- and NNE-trending structures (along with minor NNW-trending structures) display a right-lateral shear sense (**Figures 7A,B,I**), accounting for 73% of shallow strike-slip CMT solutions in the area. The N-trending structures are parallel to the FRSC and the MTJ-S, while the NNE-trending structures are parallel to the NELSC. In contrast, NE-trending structures do not display strike-slip motion; instead, these structures may be associated with pure low-magnitude normal faulting with no oblique motion. Subordinate NE-, ENE-, E-, W-, NNW-trending structures display a left-lateral shear sense (**Figures 7D–G**), accounting for 27% of the shallow strike-slip CMT solutions. The left-lateral CMTs occur near the northern plate boundary ($n = 7$), likely caused by slip between the northern microplates and the Pacific Plate, and farther to the south along the W Rift, MTJ-W, and northern FRSC ($n = 19$). Dip-slip faults also occur along the STEP fault east of the NELSC, trending NE, E, W, and WNW ($n = 12$; **Figures 7C,E–G**).

DISCUSSION: MECHANISMS OF STRIKE-SLIP FAULTING

Previous authors have suggested that the strike-slip motion in the NE Lau Basin results from strain induced by the transform motion along the northern STEP fault and asymmetric slab rollback (e.g., Hawkins, 1995; Baxter et al., 2020). This interpretation is supported by the close association of strike-slip CMTs along the boundary, extending southward to ~16°S where strike-slip CMT solutions terminate abruptly (**Figure 8**; see also Figure 5 in Baxter et al., 2020). This model suggests that there is a major, regional-scale diffuse sinistral shear zone in the NE Lau Basin with a width of approximately 120 km. Notably, there is no evidence for slip along the inferred southern boundary of the shear zone, which instead is dominated by a diffuse zone of seismicity. This is consistent with other edge-driven microplate rotation models (e.g., Schouten, 1993). On land, regional shear zones referred to as "megashears" have been interpreted to be induced by the relative motion between two plates (e.g., Arthaud and Matte, 1977; Neev et al., 1982; Campbell and Anderson, 2003) or in intra-plate settings where pre-existing weaknesses in the basement localize shearing (e.g., Frisicale et al., 2010). In these strike-slip fault systems, the fracture patterns typically follow specific geometries referred to as a Riedel shear zone, which can occur at different scales.

Here, we relate the distribution and orientation of right-lateral and left-lateral strike-slip faults within the rigid block boundaries to typical Riedel megashear mechanisms, revealing two distinct sets of structures (**Figures 9**, **10**). The first set of Riedel megashears, which we group under the name "Riedel System 1," is dominated by NNE-trending R′-shears, with minor E-trending R-shears and NNW-trending P-shears (**Figure 9**) The R'-shears are oriented at a high angle (~75°) counter-clockwise to the boundaries of the megashear zone, which trend ~95° following the orientation of the northern plate boundary. The R′-shears follow the main trends along the NELSC and the W Rift zone and are sub-parallel to MTJ-N. Typically, R′-shears may develop with or after R-shears (e.g., Atmaoui et al., 2006), which are oriented ~10–15° counter-clockwise and synthetic to the megashear zone boundaries. In the study area, R-shears are not widespread, but are sub-parallel to MTJ-W, and closely align with the structural trend of the northern Mata volcanoes and a well-developed strike-slip fault zone in the northwest map area. The P-shears are more difficult to identify but may be manifest as the WNW-trending fabrics in the southern and northern parts of the map area. Within this configuration, compression associated with σ_1 may produce the large anticline(?) associated with the NW Ridges Assemblage (**Supplementary Figure S41**) and may also result in bulging morphology of the paleo-arc crust. Extension associated with σ_3 is associated with the large ENE-trending volcanic ridges at the southern end of the NELSC, as well as West and East Mata. The orientation of these structures is oblique to the direction of hinge-rollback, suggesting that normal back-arc spreading processes cannot account for all the extension in this area. These extensional features are offset by the R-shears, creating an extensional duplex (**Figure 9**). North of the FRSC, there appears to be a cluster of NNE-trending seismicity associated with left-lateral fault motion, contrasting the right-lateral motion of faults along other NNE-trending CMTs in the region (**Figure 9B**). Sleeper and Martinez (2016) suggests that these strike-slip events are due to a zone of transferred lithosphere, although the regional kinematic control on this

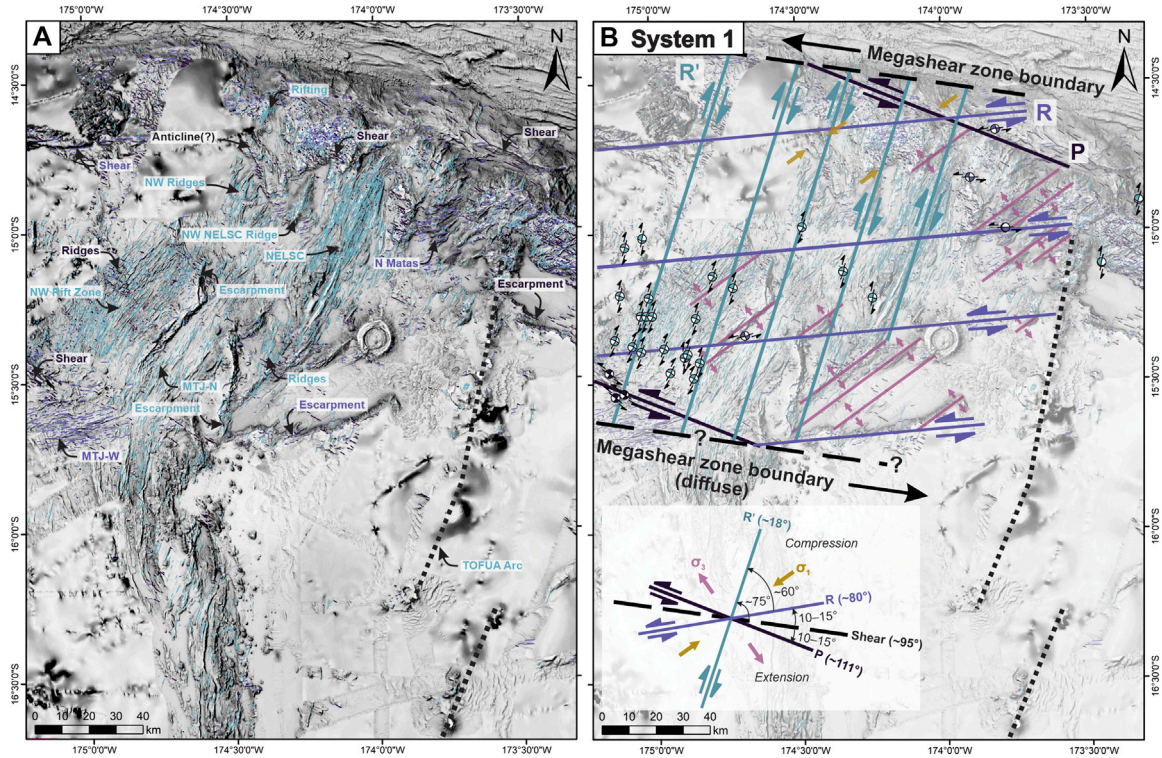

FIGURE 9 | The first set of structures overlain on TTS-shaded bathymetry: **(A)** lineaments include NNE-trending (~18°), E-trending (~80°), and WNW-trending (~111°), and are associated with numerous major structural and volcanic features in the map area (annotations as in **Figure 2**); **(B)** generalized megashear mechanism for this set of structures (Riedels System 1), with shear zone boundaries oriented ~98°, dominated by NNE-trending R′-shears (R-lateral). Extension associated with σ_3 is offset by R-shears (L-lateral) and is also associated with large volcanic ridges across the map. Active seismicity (CMTs) is mainly restricted to the western map area, extending south to a diffuse boundary (dashed line). Bathymetric compilation as in **Figure 3**.

reversal is unclear. We therefore interpret the southernmost *diffuse* boundary of the megashear zone to occur near Escarpment B (**Figures 5**, **9B**).

The second set of Riedel megashears are similar but rotated ~8–12° counter-clockwise relative to the first set of shears, which we group under the name "Riedel System 2" (**Figure 10**). These shears are dominated by N-trending R′-shears, with minor ENE-trending R-shears and W-trending P-shears. The R′-shears follow the orientation of MTJ-S and FRSC, the N-trending fissure system extending north of the Niuatahi volcano, and other N-trending features in the area, including the area of extension labeled "Rifting" on **Figures 5**, **10A**. The R-shears follow the trend of the West Mata and East Mata volcanoes and the large volcanic ridge to the southwest of Niuatahi, apparently re-activating previous extensional fabric. The megashear zone boundaries trend ~80°, following the previous orientation of R-shears in System 1 (**Figure 9B**), and sub-parallel to the orientation of Escarpment B in the south (dashed lines in **Figure 10**). P-shears are also poorly defined for this configuration, but match strike-slip faulting near the northern and southern boundaries of the megashear zone. In this configuration, extension along σ_3 is associated with NE-trending volcanic ridges across the map area, such as the western Mata volcanoes, which are offset by R-shears. This extensional fabric is also parallel to the MTJ-N, the West Rift zone, and the northern and southern terminations of the NELSC and may be enhancing spreading associated with hinge-rollback.

The differing distribution of fault populations from a typical Riedel shear zone (dominated by R-shears) is likely because R′-shears occur at an angle similar to that of faults produced by earlier back-arc extension. It is easier to reactivate these pre-existing faults as opposed to creating new ones as the stress required for frictional sliding along pre-existing faults is much less than the fracture strength (e.g., Byerlee, 1978). Similarly, as the stress-field rotated, pre-existing extensional faults were re-activated as R-shears. This effect has been observed in other back-arc basins (e.g., Manus Basin: Martinez and Taylor, 1996; Morley et al., 2004; Maestro-González et al., 2008). Faults that have undergone strike-slip reactivation tend to have zig-zag geometries with little throw. These morphologies are common throughout the map area but are particularly well-defined in the western part of the map area in the West Rift zone and the MTJ-W arm. Therefore, the observed strike-slip kinematics in the study area support a rigid block model of lithospheric-scale Riedel (mega) shearing, where shearing reactivates pre-existing extensional faults. This indicates that structures in megashear zones may be predisposed to align themselves to the pre-existing fabrics in back-arc settings. Since the tensional stresses in this region are

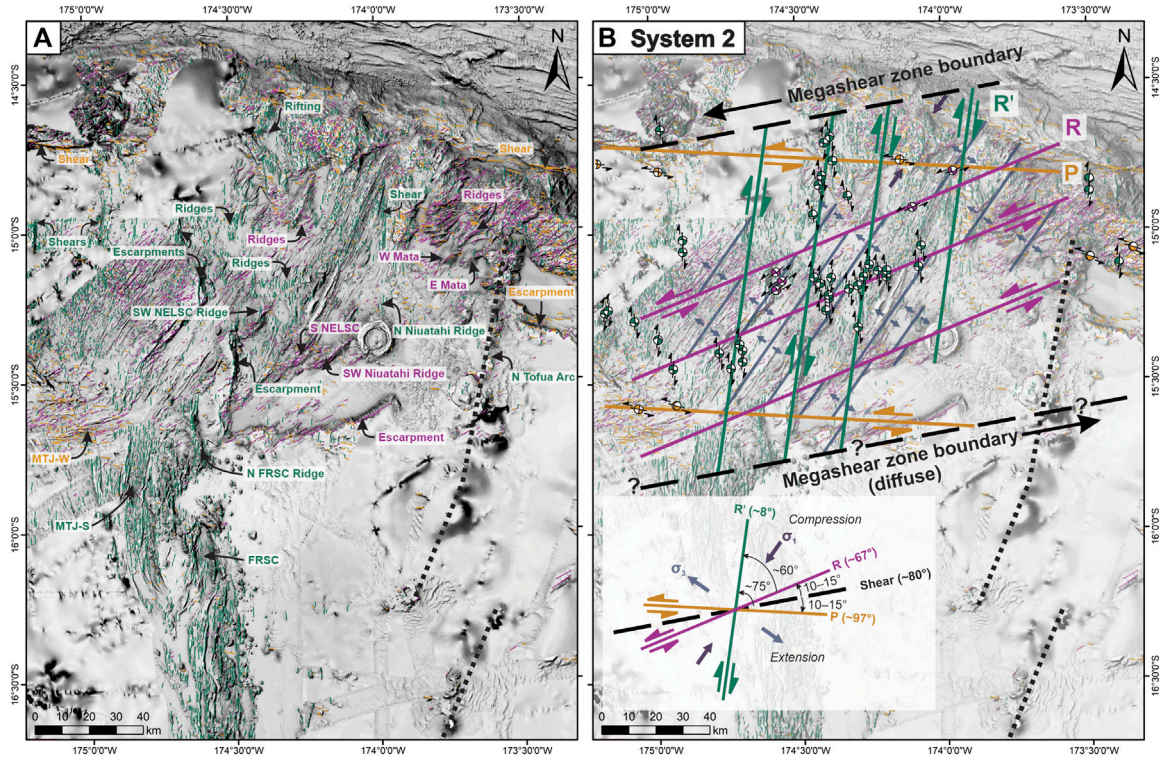

FIGURE 10 | The second set of structures overlain on TTS-shaded bathymetry: **(A)** lineaments include N-trending (~8°), ENE-trending (~67°), and W-trending (~97°), and are associated with numerous major structural and volcanic features in the map area (annotations as in **Figure 2**); **(B)** generalized megashear mechanism for this set of structures (Riedels System 2), with shear zone boundaries rotated counter-clockwise to ~80°, dominated by N-trending R′-shears (R-lateral). Extension associated with σ_3 is offset by R-shears (L-lateral) and is also associated with large volcanic ridges across the map. Active seismicity (CMTs) dominates the central map area closer to the arc, extending south to a diffuse boundary (dashed line). Bathymetric compilation as in **Figure 3**.

accommodated by re-activation of normal faults as strike-slip faults, other large-scale strike-slip features (such as large-scale drag features) do not manifest in the map view of the area.

Structures associated with both Riedel systems 1 and 2 are distributed across the map area; however, cross-cutting relationships indicate that System 1 structures only cross-cut themselves, while System 2 structures cross-cut both themselves and System 1 structures (**Table 1**; **Figures 6C,D**), indicating that the System 2 structures formed later. In addition, the distribution of modern seismicity revealed by CMTs provides some insight into the timing of Riedel megashear formation. Active seismicity associated with System 1 megashears occurs mainly in the western portion of the map area (light blue beach balls in **Figure 9B**), while seismicity associated System 2 megashears occurs in the central part of the map area closest to the volcanic arc (green and pink beach balls in **Figure 10B**). Therefore, we propose that System 1 megashear structures formed first, encompassing the entire map area. This was followed by System 2 megashear structures. Currently, both configurations remain active in the different regions of the study area. Therefore, we propose that occurrence of two different Riedel megashear geometries in the NE Lau Basin (Systems 1 and 2; **Figures 9B**, **10B**) is associated with a counterclockwise rotation of the stress field over time. In general, the geometry and kinematics of the back-arc structures support the idea of a megashear zone, driven by the relative motion between the plates. Additional work is needed to understand the geodynamic controls on the changing stress field throughout the map area.

DISCUSSION: CONSEQUENCES OF STRESS-FIELD ROTATION

In the NE Lau Basin, the counterclockwise rotation of the stress field is associated with a change in the orientation of the extensional axis along a new northward trend. As the extensional axis changes, there is a tendency for rifts to propagate outwards from the tips along the new extensional axis (e.g., CLSC: Parson et al., 1990). This process may be quicker when propagation occurs in thinner crust and where back-arc extension is the greatest associated with fast rates of trench retreat (Parson et al., 1990). This structural reconfiguration may have induced the propagation of new rifts, such as FRSC segments, which are interpreted to be the youngest features in the NE Lau Basin (Schmid et al., 2020). Microseismicity at the southern tip of the FRSC indicates ongoing southward propagation of this rift toward the

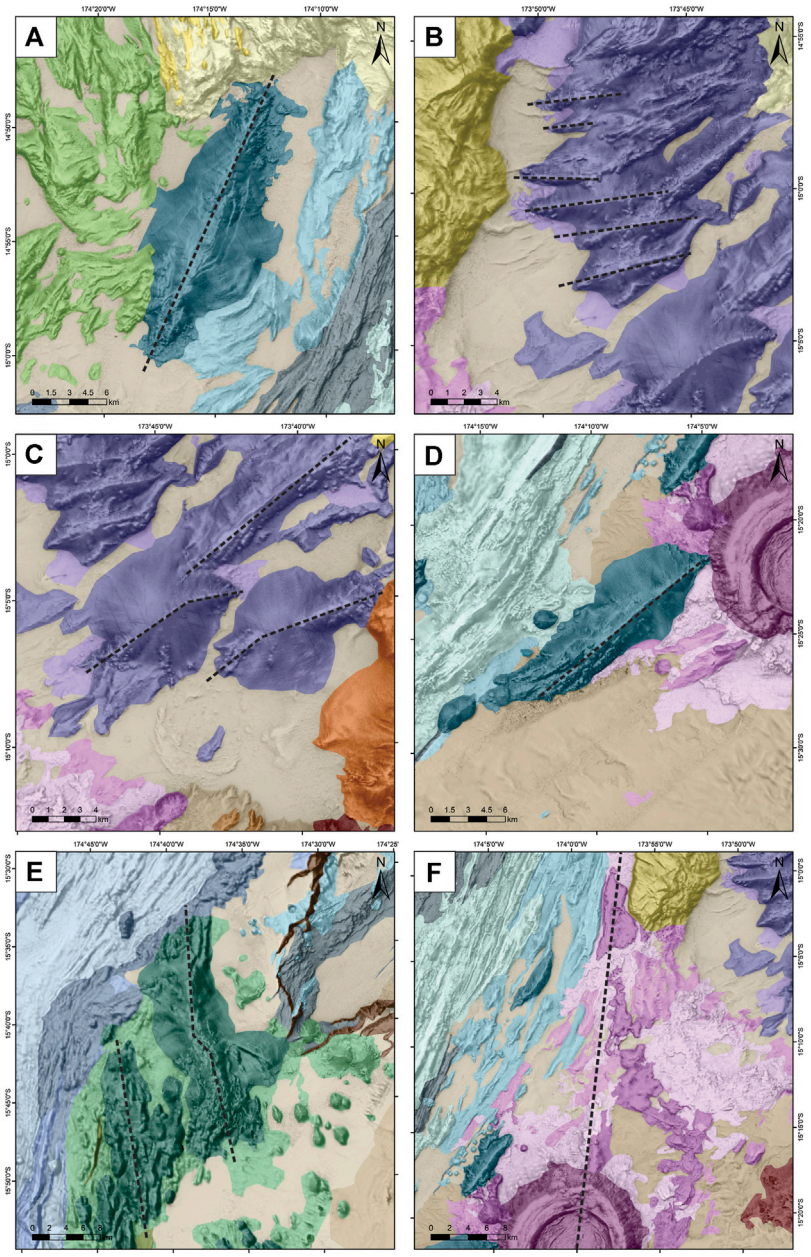

FIGURE 11 | Examples of large off-axis volcanic ridges/fissures in the study area aligned along different orientations: **(A)** NNE-trending ridge located northwest of the NELSC; **(B)** E-trending ridges of the northern Mata volcanoes; **(C)** ENE-trending ridges of West Mata and East Mata volcanoes; **(D)** ENE-trending ridge located southwest of Niuatahi; **(E)** N-trending ridges north of the FRSC; and **(F)** small N-trending ridge and fissure system north of Niuatahi. Bathymetric compilation as in **Figure 3**, geology map follows the legend in **Figure 5**.

volcanic arc (Schmid et al., 2021). There may also be simultaneous northward propagation of the FRSC and southward propagation of the MTJ-S (**Figure 5**). In the area where these two spreading centers overlap, we observe oblique and curved structural patterns and active seismicity (e.g., North Fiji Basin: Ruellan et al., 1994; Conder and Wiens, 2011). In addition, within the map area, N-trending rifting is occurring along the paleo-arc crust in the northern part of the map area (labeled "Rifting" in **Figure 5**). These structures may reflect the early stages of rift propagation, but higher-resolution magnetic data is needed to investigate the nature of these features. Ongoing rift propagation is interpreted along the northern and southern tips of the NELSC. The northern end is associated with a NE-trending V-shaped rift tip and active normal faulting (**Figures 5**, **7C**), while the southern NELSC displays a SW-trending V-shaped rift tip bound by steep-walled escarpments (Escarpment B and C in **Figure 5**). The propagation of these NE- and SW-trending rift tips may be enhanced by σ_3 extension

TABLE 2 | Volcanic features associated with enhanced magmatism in the map area and structural association in relation to Riedel Systems 1 and 2 (**Figures 9**, **10**).

Volcanic feature	Orientation	Structural association
Northwestern NELSC volcanic ridge (**Figure 11A**)	NNE trending	R′-shears in System 1 (**Figure 9**)
Northern Mata volcanoes (**Figure 11B**)	E-trending	R-shears in System 1 (**Figure 9**)
West Mata and East Mata valcanoes (**Figure 11E**), Southwestern Niuatahi volcanic ridge (**Figure 11F**)	ENE-trending	σ_3 extension in System 1 (**Figure 9**), reactivated R-shears in System 2 (**Figure 10**)
North FRSC volcanic ridge (**Figure 11C**), volcanic ridge and fissure system north of Niuatahi (**Figure 11D**)	N-trending	Trench-parallel back-arc extension, R′-shears in System 2 (**Figure 10**)
Enhanced magmatism along southern NELSC, MTJ-N (**Figure 5**)	NE-trending	σ_3 extension in System 2 (**Figure 10**)
Niuatahi volcano (**Figure 5**)	N/A	Intersection of R′-shear and R-shear in System 2 (**Figure 10**)

in the reconfigured (System 2) stress field, in addition to slab rollback (**Figure 10B**).

The re-orientation of the stress field has mainly affected the area closest to the arc, preserving the original megashear zone configuration in the west where it remains seismically active (**Figure 9B**). This could indicate that the eastern portion of the NE Lau Basin may be in the nascent stages of nanoplate emergence, proposed by Conder and Wiens (2011) as the separate "Niuatoputapu" plate. This is supported by a drastic change in the structural fabric of the basin from west to east across Escarpment C (**Figures 5**–**7**). The fabric to the west of this escarpment is dominated by zig-zagging normal-faulted terrane of the West Rift assemblage, and to the east of this escarpment are the N- and NNE-trending volcanic ridges of the NW Ridges and NELSC assemblages. Like other back-arc micro- and nanoplates, the precise boundaries of Niuatoputapu are difficult to define, and may remain only partially separated, as is the case in the southern diffuse boundary of the Niuafo'ou microplate (**Figure 2**; Sleeper and Martinez, 2016). This work demonstrates an important mechanism for the emergence of new micro- or nano-plates in back-arc environments; namely, the propagation of new rifts in response to a rotating stress field.

Discussion: Structural Controls on Magmatic-Hydrothermal Activity

One of the most striking features of the NE Lau Basin is the decentralized nature of volcanism on the seafloor, manifest by large off-axis volcanic ridges, hydrothermally active rear-arc volcanoes, and widespread lava flows (**Figure 5**). Previous authors propose that the Mata rear-arc volcanoes are controlled by small crustal tears linked to strike-slip faulting along the STEP fault (Govers and Wortel, 2005; Embley et al., 2009), but these authors do not provide an explanation for the variable orientations of the Mata volcanoes, along with other enigmatic features such as the siting of the large Niuatahi volcano. The structural framework outlined here provides insight into the occurrence of many of these seafloor features. Notably, large off-axis volcanic ridges reflect areas of enhanced magmatism in the map area (**Figure 11**) and are aligned along four main orientations: 1) NNE-trending ridges, including the NW NELSC Ridge (**Figure 11A**); 2) E-trending ridges forming the northern Mata volcanoes (**Figure 11B**); 3) ENE-trending ridges, including the West Mata and East Mata volcanoes (**Figure 11C**) and the SW Niuatahi Ridge (**Figure 11D**); and 4) N-trending ridges, including the N FRSC Ridge (**Figure 11E**) and the subtle ridge and fissure system (and associated lava flows) extending N of Niuatahi (**Figure 11F**; Embley and Rubin, 2018). In addition to these off-axis features, we note enhanced magmatism along the southern NELSC, indicated by elevated topography relative to the rest of the NELSC (**Figure 5**). The MTJ-N is characterized by a wide neovolcanic zone relative to the MTJ-S or other spreading centers, which may also indicate enhanced magmatism (**Figure 5**). The association of each of these volcanic features with the major structures identified in this study are shown in **Table 2**. Notably, magmatism appears to be closely related to the occurrence and geometry of the Riedel shear systems, including R-shears, R′-shears and σ_3 extension. In addition, the intersection of a N-trending structure (R′-shear in System 2) and NNE-trending structure (R-shear in System 2) provides a structural conduit to focus magmatism in the rear-arc to form the Niuatahi volcano. These two structures, which have not been previously described, are underlain by linear magnetic anomalies (Austin, 2012), indicating that magma is exploiting these structural pathways. Across the map area, hydrothermal vents are closely associated with these regions of enhanced magmatism (**Figure 5**). Continual re-activation of faults may ensure that these pathways remain permeable despite precipitation of secondary hydrothermal minerals. This complex structural configuration, combined with unusually high upper mantle temperatures and ultrafast subduction rates (e.g., Regelous, 2008), provides the basis for diverse lithologies and eruption styles in the basin, along with a range of style and composition of hydrothermal venting (e.g., Embley and Rubin, 2018; Chadwick et al., 2019).

CONCLUSION

Compared to mid-ocean ridges, back-arc spreading centers are ephemeral features that evolve dynamically in response to convergence, subduction-zone collisions, and microplate interactions, among others. The NE Lau Basin is characterized by extreme tectonic complexity, associated with fast convergence rates, high upper mantle temperatures, and thin oceanic crust (Bevis, et al., 1995; Conder and Wiens, 2011; Embley et al., 2018), producing diverse lithologies and eruption styles in the rear-arc and back-arc regions (e.g., Embley and Rubin, 2018). This

complexity is manifest as seafloor fabrics with variably oriented structures. The observed structural patterns reflect the interplay between extension associated with slab-rollback and strike-slip tectonics along the northern STEP fault, with shallow-crustal strike-slip faulting extending over ~120 km from the STEP fault. Two distinct sets of structures associated with Riedel shear mechanisms are described for the first time, indicating a recent counterclockwise rotation of the stress field that primarily affects the region closest to the arc. The structural configurations highlight the importance of re-activation of earlier-formed structures during rotation of the stress-field. The structures that formed and were re-activated in this megashear zone account for the orientations of many of the previously-enigmatic seafloor features observed, such as the Mata volcanoes and large off-axis volcanic ridges. This study provides important constraints on the geologic and structural evolution of the NE Lau Basin, including the tectonic controls on enhanced magmatism in rear-arc and off-axis regions, as well as the distribution of hydrothermal vent sites in the region.

DATA AVAILABILITY STATEMENT

The following bathymetric datasets can be found in the Rolling Deck to Repository (R2R): FK171110: https://doi.org/10.7284/907642; KM1024: https://doi.org/10.7284/900840; and KM1129: https://doi.org/10.7284/903993. The SO-263 bathymetric dataset can be found in PANGAEA: https://doi.pangaea.de/10.1594/PANGAEA.892778. The CMT dataset for this study can be found in the Global Centroid-Moment-Tensor database by Dziewonski et al. (1981) and Ekström et al. (2012): www.globalcmt.org.

AUTHOR CONTRIBUTIONS

MA prepared all figures, drafted the main text, made equal contributions to the interpretation of the data, and supervised the M.Sc. thesis by CN-J. CN-J completed preliminary data collection, made equal contributions to the interpretation of the data as part of an M.Sc. thesis. KR secured funding for FK171110 (chief scientist), contributed to bathymetric data collection, interpretation, and editing of the drafts. KH secured funding for SO-263 (chief scientist), contributed to interpretation and editing of drafts. MH contributed to interpretations and did substantial editing of drafts. AB contributed to developing methodology for CMT interpretation, interpretation of data, and editing of drafts. MS Contributed to interpretations and editing of drafts.

FUNDING

The funding for the project 03G0263 by the German Bundesministerium für Bildung und Forschung is gratefully acknowledged. We acknowledge the support of the Schmidt Ocean Institute for access to the R/V Falkor and ROV SuBastian on cruise FK171110. MA acknowledges funding from NSERC-DG and the Connaught New Researcher program (UofT). MA, MH, and MS acknowledge funding from the NSERC-CREATE iMAGE program. KR acknowledges funding from NSF (NSF-1538121). This is contribution MERC-ME-2020-003 to the modern-ancient crust project of the Canadian Metal Earth program. This is SOEST publication #11345.

ACKNOWLEDGMENTS

We appreciate the efforts of the SO-263 Shipboard Scientific Party, ROV QUEST team, and Captain O. Meyer and his crew on R/V Sonne for their contributions and support. We also thank the FK171110 Shipboard Scientific Party and crew of the R/V Falkor, and the support of the Schmidt Ocean Institute. We gratefully acknowledge S. Merle for processing and compiling the bathymetric data from Rubin and Shipboard Scientific Party (2010), Martinez and Shipboard Scientific Party (2013), and Rubin and Shipboard Scientific Party (2018), and S. Panasiuk for her assistance with bathymetric post-processing using the TTS-shader. We acknowledge L. Calhoun for valuable feedback on the structural interpretations. Finally, we thank the reviewers for this manuscript, who greatly enhanced its overall clarity.

SUPPLEMENTARY MATERIAL

The Supplementary Material for this article can be found online at: https://www.frontiersin.org/articles/10.3389/feart.2021.665185/full#supplementary-material

REFERENCES

Anderson, M. O., Chadwick, W. W., Jr., Hannington, M. D., Merle, S. G., Resing, J. A., Baker, E. T., et al. (2017). Geological Interpretation of Volcanism and Segmentation of the Mariana Back-Arc Spreading Center Between 12.7°N and 18.3°N. *Geochem. Geophys. Geosyst.* 18, 2240–2274. doi:10.1002/2017GC006813

Anderson, M. O., Hannington, M. D., Haase, K., Schwarz-Schampera, U., Augustin, N., McConachy, T. F., et al. (2016). Tectonic Focusing of Voluminous Basaltic Eruptions in Magma-Deficient Backarc Rifts. *Earth Planet. Sci. Lett.* 440, 43–55. doi:10.1016/j.epsl.2016.02.002

Arthaud, F., and Matte, P. (1977). Late Paleozoic Strike-Slip Faulting in Southern Europe and Northern Africa: Result of a Right-Lateral Shear Zone between the Appalachians and the Urals. *Bull. Geol. Soc. Am.* 88, 1305–1320. doi:10.1130/0016-7606(1977)88<1305:LPSFIS>2.0.CO;2

Aruculus, R., and Shipboard Scientific Party (2004). *Voyage Summary SS06/2004: Submarine Volcanic and Hydrothermal Activity in the New Hebrides Arc-Backarc System*. Hobart, Australia: CSIRO. Available at: http://www.cmar.csiro.au/datacentre/process/data_files/cruise_docs/ss2004_v06_summary.pdf.

Atmaoui, N., Kukowski, N., Stöckhert, B., and König, D. (2006). Initiation and Development of Pull-Apart Basins With Riedel Shear Mechanism: Insights From Scaled Clay Experiments. *Int. J. Earth Sci.* 95, 225–238. doi:10.1007/s00531-005-0030-1

Augustin, N., van der Zwan, F. M., Devey, C. W., Ligi, M., Kwasnitschka, T., Feldens, P., et al. (2016). Geomorphology of the Central Red Sea Rift: Determining Spreading Processes. *Geomorphology* 274, 162–179. doi:10.1016/j.geomorph.2016.08.028

Austin, R. A. (2012). Early Seafloor Spreading and Variations in Crustal Accretion in the Lau Basin. Doctoral dissertation. Honolulu (HI): University of Hawaii at Manoa. Available at: https://scholarspace.manoa.hawaii.edu/handle/10125/100916.

Baker, E. T., Walker, S. L., Massoth, G. J., and Resing, J. A. (2019). The NE Lau Basin: Widespread and Abundant Hydrothermal Venting in the Back-Arc Region Behind a Superfast Subduction Zone. *Front. Mar. Sci.* 6, 382. doi:10.3389/fmars.2019.00382

Baxter, A. T., Hannington, M. D., Stewart, M. S., Emberley, J. M., Breker, K., Krätschell, A., et al. (2020). Shallow Seismicity and the Classification of Structures in the Lau Back-Arc Basin. *Geochem. Geophys. Geosyst.* 21, e2020GC008924. doi:10.1029/2020GC008924

Beaulieu, S. E., and Szafranski, K. (2019). InterRidge Global Database of Active Submarine Hydrothermal Vent Fields, Version 3.4. Available at: http://vents-data.interridge.org.

Bevis, M., Taylor, F. W., Schutz, B. E., Recy, J., Isacks, B. L., Helu, S., et al. (1995). Geodetic Observations of Very Rapid Convergence and Back-Arc Extension at the Tonga Arc. *Nature* 374, 249–251. doi:10.1038/374249a0

Bird, P. (2003). An Updated Digital Model of Plate Boundaries. *Geochem. Geophys. Geosyst.* 4, 1027. doi:10.1029/2001GC000252

Birner, S. K., Warren, J. M., Cottrell, E., Davis, F. A., Kelley, K. A., and Falloon, T. J. (2017). Forearc Peridotites From Tonga Record Heterogeneous Oxidation of the Mantle Following Subduction Initiation. *J. Petrol.* 58, 1755–1780. doi:10.1093/petrology/egx072

Brens, R., Liu, X.-M., Turner, S., and Rushmer, T. (2018). Lithium Isotope Variations in Tonga-Kermadec Arc-Lau Back-Arc Lavas and Deep Sea Drilling Project (DSDP) Site 204 Sediments. *Isl. Arc* 28, e12276. doi:10.1111/iar.12276

Brown, L. (2014). "Texture Shading: A New Technique for Depicting Terrain Relief," in Paper Presented at the 15th ICA Mountain Cartography Workshop, Banff, Canada, April 22–26, 2014, International Cartographic Association (ICA). Available at: https://app.box.com/v/textureshading (Accessed May 18, 2020).

Buck, W. R. (2004). "Consequences of Asthenospheric Variability on Continental Rifting," in *Rheology and Deformation of the Lithosphere at Continental Margins*. Editor G. D. Karner (New York, NY: Columbia University Press), 1–30.

Buck, W. R., Lavier, L. L., and Poliakov, A. N. B. (2005). Modes of Faulting at Mid-Ocean Ridges. *Nature* 434, 719–723. doi:10.1038/nature03358

Buck, W. R. (2006). "The Role of Magma in the Development of the Afro-Arabian Rift System," *Afar Volcanic Province Within the East African Rift System*. Editors G. Yirgu, C. J. Ebinger, and P. K. H. Maguire (London, United Kingdom: Geological Society of London Special Publication), Vol. 259, 43–54.

Byerlee, J. (1978). Friction of Rocks. *Pure Appl. Geophys.* 116, 615–626. doi:10.1007/BF00876528

Campbell, P. A., and Anderson, T. H. (2003). Structure and Kinematics Along a Segment of the Mojave-Sonora Megashear: A Strike-Slip Fault that Truncates the Jurassic Continental Magmatic Arc of Southwestern North America. *Tectonics* 22, 1077. doi:10.1029/2002TC001367

Chadwick, W. W., Jr., Rubin, K. H., Merle, S. G., Bobbitt, A. M., Kwasnitschka, T., and Embley, R. W. (2019). Recent Eruptions Between 2012 and 2018 Discovered at West Mata Submarine Volcano (NE Lau Basin, SW Pacific) and Characterized by New Ship, AUV, and ROV Data. *Front. Mar. Sci.* 6, 495. doi:10.3389/fmars.2019.00495

Chase, C. G. (1978). Extension Behind Island Arcs and Motions Relative to Hot Spots. *J. Geophys. Res.* 83 (B11), 5385–5387. doi:10.1029/JB083iB11p05385

Conder, J. A., and Wiens, D. A. (2011). Shallow Seismicity and Tectonics of the central and Northern Lau Basin. *Earth Planet. Sci. Lett.* 304, 538–546. doi:10.1016/j.epsl.2011.02.032

Dale, C. W., Macpherson, C. G., Pearson, D. G., Hammond, S. J., and Arculus, R. J. (2012). Inter-Element Fractionation of Highly Siderophile Elements in the Tonga Arc Due to Flux Melting of a Depleted Source. *Geochim. Cosmochim. Acta* 89, 202–225. doi:10.1016/j.gca.2012.03.025

Danyushevsky, L. V., Falloon, T. J., Sobolev, A. V., Crawford, A. J., Carroll, M., and Price, R. C. (1993). The H2O Content of Basalt Glasses From Southwest Pacific Back-Arc Basins. *Earth Planet. Sci. Lett.* 117, 347–362. doi:10.1016/0012-821X(93)90089-R

Dril, S. I., Kuzmin, M. I., Tsipukova, S. S., and Zonenshain, L. P. (1997). Geochemistry of Basalts From the Western Woodlark, Lau and Manus Basins: Implications for Their Petrogenesis and Source Rock Compositions. *Mar. Geol.* 142, 57–83. doi:10.1016/S0025-3227(97)00041-8

Dziewonski, A. M., Chou, T.-A., and Woodhouse, J. H. (1981). Determination of Earthquake Source Parameters From Waveform Data for Studies of Global and Regional Seismicity. *J. Geophys. Res.* 86 (B4), 2825–2852. doi:10.1029/JB086iB04p02825

Ebinger, C. J., van Wijk, J., and Kier, D. (2013). "The Time Scales of continental Rifting: Implications for Global Processes," in *The Web of Geological Sciences: Advances, Impacts, and Interactions*. Editor M. E. Bickford (London, United Kingdom: Geological Society of America Special Publication), Vol. 500, 1–28.

Eguchi, T., Fujinawa, Y., and Ukawa, M. (1989). Microearthquakes and Tectonics in an Active Back-Arc Basin: The Lau Basin. *Phys. Earth Planet. Inter.* 56, 210–229. doi:10.1016/0031-9201(89)90158-1

Ekström, G., Nettles, M., and Dziewoński, A. M. (2012). The Global CMT Project 2004-2010: Centroid-Moment Tensors for 13,017 Earthquakes. *Phys. Earth Planet. Inter.* 200–201, 1–9. doi:10.1016/j.pepi.2012.04.002

Embley, R. W., Merle, S. G., Lupton, J. E., Resing, J., Baker, E. T., Lilley, M. D., Arculus, R. J., and Crowhurst, P. V. (2009). "Extensive and Diverse Sumbarine Volcanism and Hydrothermal Activity in the NE Lau Basin," in Paper Presented at the American Geophysical Union Fall Meeting 2009, San Francisco, CA, december 14–18, 2009, American Geophysical Union (AGU). Available at: https://ui.adsabs.harvard.edu/abs/2009AGUFM.V51D1719E/abstract (Accessed May 18, 2020).

Embley, R. W., and Rubin, K. H. (2018). Extensive Young Silicic Volcanism Produces Large Deep Submarine Lava Flows in the NE Lau Basin. *Bull. Volcanol.* 80, 36. doi:10.1007/s00445-018-1211-7

Escrig, S., Bézos, A., Langmuir, C. H., Michael, P. J., and Arculus, R. (2012). Characterizing the Effect of Mantle Source, Subduction Input and Melting in the Fonualei Spreading Center, Lau Basin: Constraints on the Origin of the Boninitic Signature of the Back-Arc Lavas. *Geochem. Geophys. Geosyst.* 13, 10008. doi:10.1029/2012GC004130

Ewart, A., Collerson, K. D., Regelous, M., Wendt, J. I., and Niu, Y. (1998). Geochemical Evolution Within the Tonga-Kermadec-Lau Arc-Back-Arc Systems: The Role of Varying Mantle Wedge Composition in Space and Time. *J. Petrol.* 39, 331–368. doi:10.1093/petroj/39.3.331

Falloon, T. J., and Crawford, A. J. (1991). The Petrogenesis of High-Calcium Boninite Lavas Dredged From the Northern Tonga Ridge. *Earth Planet. Sci. Lett.* 102, 375–394. doi:10.1016/0012-821X(91)90030-L

Falloon, T. J., Danyushevsky, L. V., Crawford, T. J., Maas, R., Woodhead, J. D., Eggins, S. M., et al. (2007). Multiple Mantle Plume Components Involved in the Petrogenesis of Subduction-Related Lavas From the Northern Termination of the Tonga Arc and Northern Lau Basin: Evidence From the Geochemistry of Arc and Backarc Submarine Volcanics. *Geochem. Geophys. Geosyst.* 8, Q09003. doi:10.1029/2007GC001619

Falloon, T. J., Green, D. H., and Crawford, A. J. (1987). Dredged Igneous Rocks From the Northern Termination of the Tofua Magmatic Arc, Tonga and Adjacent Lau basin. *Aust. J. Earth Sci.* 34, 487–506. doi:10.1080/08120098708729428

Falloon, T. J., Malahoff, A., Zonenshaina, L. P., and Bogdanova, Y. (1992). Petrology and Geochemistry of Back-Arc Basin Basalts From Lau Basin Spreading Ridges at 15°, 18° and 19°S. *Mineral. Petrol.* 47, 1–35. doi:10.1007/BF01165295

Frisicale, M. C., Dimieri, L. V., Araujo, V. S., and Dristras, J. A. (2010). Deformation Mechanisms in the Mylonite/Striped Gneiss and Mylonite/Ultramylonite Transition in Sierras de Azul, Rio de la Plata Craton, Buenos Aires. *Rev. Asoc. Geol. Argent.* 67, 4–18.

GEBCO Compilation Group (2019). Data From: GEBCO 2019 Grid. Available at https://www.gebco.net/data_and_products/gridded_bathymetry_data/ (Accessed January 1, 2021). doi:10.5285/a29c5465-b138-234d-e053-6c86abc040b9

Global Volcanism Program (2013). *Volcanoes of the World, v. 4.8.6*. Editor E. Venzke (Washington, DC: Smithsonian Institution).

Govers, R., and Wortel, M. J. R. (2005). Lithosphere Tearing at Step Faults: Response to Edges of Subduction Zones. *Earth Planet. Sci. Lett.* 236, 505–523. doi:10.1016/j.epsl.2005.03.022

Haase, K., and Shipboard Scientific Party (2018). "SO-263 Cruise Report Tonga Rift," in *Wochenberichte und Short Cruise Reports*. Hamburg, Germany: Universität Hamburg. Available at: https://www.ldf.uni-hamburg.de/sonne/wochenberichte/wochenberichte-sonne/so263-265/so263-scr.pdf.

Hahm, D., Hilton, D. R., Castillo, P. R., Hawkins, J. W., Hanan, B. B., and Hauri, E. H. (2012). An Overview of the Volatile Systematics of the Lau Basin – Resolving the Effects of Source Variation, Magmatic Degassing and Crustal Contamination. *Geochim. Cosmochim. Acta* 85, 88–113. doi:10.1016/j.gca.2012.02.007

Hall, R. (2002). Cenozoic Geological and Plate Tectonic Evolution of SE Asia and the SW Pacific: Computer-Based Reconstructions, Model and Animations. *J. Asian Earth Sci.* 20, 353–431. doi:10.1016/S1367-9120(01)00069-4

Hawkins, J. W. (1995). "The Geology of the Lau Basin," in *Backarc Basins: Tectonics and Magmatism*. Editor B. Taylor (New York, NY: Plenum Press), 63–138.

Heuret, A., and Lallemand, S. (2005). Plate Motions, Slab Dynamics and Back-Arc Deformation. *Phys. Earth Planet. Inter.* 149, 31–51. doi:10.1016/j.pepi.2004.08.022

Hilton, D. R., Hammerschmidt, K., Loock, G., and Friedrichsen, H. (1993). Helium and Argon Isotope Systematics of the Central Lau Basin and Valu Fa Ridge: Evidence of Crust/Mantle Interactions in a Back-Arc Basin. *Geochim. Cosmochim. Acta* 57, 2819–2841. doi:10.1016/0016-7037(93)90392-A

Honda, M., Patterson, D. B., McDougall, I., and Falloon, T. J. (1993). Noble Gases in Submarine Pillow Basalt Glasses From the Lau Basin: Detection of a Solar Component in Backarc Basin Basalts. *Earth Planet. Sci. Lett.* 120, 135–148. doi:10.1016/0012-821X(93)90235-2

Ito, G., and Behn, M. D. (2008). Magmatic and Tectonic Extension at Mid-Ocean Ridges: 2. Origin of Axial Morphology. *Geochem. Geophys. Geosyst.* 9, Q09O12. doi:10.1029/2008GC001970

Karig, D. E. (1970). Ridges and Basins of the Tonga-Kermadec Island Arc System. *J. Geophys. Res.* 75, 239–254. doi:10.1029/JB075i002p00239

Keller, N. S., Arculus, R. J., Hermann, J., and Richards, S. (2008). Submarine Back-Arc Lava With Arc Signature: Fonualei Spreading Center, Northeast Lau Basin, Tonga. *J. Geophys. Res.* 113, B08S07. doi:10.1029/2007JB005451

Kendrick, M. A., Danyushevsky, L. V., Falloon, T. J., Woodhead, J. D., Arculus, R. J., and Ireland, T. (2020). SW Pacific Arc and Backarc Lavas and the Role of Slab-Bend Serpentinites in the Global Halogen Cycle. *Earth Planet. Sci. Lett.* 530, 115921. doi:10.1016/j.epsl.2019.115921

Kim, J., Son, S.-K., Son, J.-W., Kim, K.-H., Shim, W. J., Kim, C. H., et al. (2009). Venting Sites Along the Fonualei and Northeast Lau Spreading Centers and Evidence of Hydrothermal Activity at an Off-Axis Caldera in the Northeastern Lau Basin. *Geochem. J.* 43, 1–13. doi:10.2343/geochemj.0.0164

Klischies, M., Petersen, S., and Devey, C. W. (2019). Geological Mapping of the Menez Gwen Segment at 37°50′N on the Mid-Atlantic Ridge: Implications for Accretion Mechanisms and Associated Hydrothermal Activity at Slow-Spreading Mid-Ocean Ridges. *Mar. Geol.* 412, 107–122. doi:10.1016/j.margeo.2019.03.012

Langmuir, C. H., Bézos, A., Escrig, S., and Parman, S. W. (2006). "Chemical Systematics and Hydrous Melting of the Mantle in Back-Arc Basins," in *Back-Arc Spreading Systems: Geological, Biological, Chemical, and Physical Interactions*. Editors D. M. Christie, C. R. Fisher, S.-M. Lee, and S. Givens (Washington, DC: American Geophysical Union, Geophysical Monograph Series), Vol. 166, 87–146.

Layne, G. D., Kent, A. J. R., and Bach, W. (2009). δ37Cl Systematics of a Backarc Spreading System: The Lau Basin. *Geology* 37, 427–430. doi:10.1130/G25520A.1

Loock, G., McDonough, W. F., Goldstein, S. L., and Hofmann, A. W. (1990). Isotopic Compositions of Volcanic Glasses from the Lau Basin. *Mar. Min.* 9, 235–245.

Lupton, J. E., Arculus, R. J., Evans, L. J., and Graham, D. W. (2012). Mantle Hotspot Neon in Basalts From the Northwest Lau Back-Arc Basin. *Geophys. Res. Lett.* 39, L08308. doi:10.1029/2012GL051201

Lupton, J. E., Arculus, R. J., Greene, R. R., Evans, L. J., and Goddard, C. I. (2009). Helium Isotope Variations in Seafloor Basalts From the Northwest Lau Backarc Basin: Mapping the Influence of the Samoan Hotspot. *Geophys. Res. Lett.* 36, L17313. doi:10.1029/2009GL039468

Lupton, J., Rubin, K. H., Arculus, R., Lilley, M., Butterfield, D., Resing, J., et al. (2015). Helium Isotope, C/3He, and Ba-Nb-Ti Signatures in the Northern Lau Basin: Distinguishing Arc, Back-Arc, and Hotspot Affinities. *Geochem. Geophys. Geosyst.* 16, 1133–1155. doi:10.1002/2014GC005625

Lytle, M. L., Kelley, K. A., Hauri, E. H., Gill, J. B., Papia, D., and Arculus, R. J. (2012). Tracing Mantle Sources and Samoan Influence in the Northwestern Lau Back-Arc basin. *Geochem. Geophys. Geosyst.* 13, Q10019. doi:10.1029/2012GC004233

Macdonald, K. C. (1982). Mid-Ocean Ridges: Fine Scale Tectonic, Volcanic and Hydrothermal Processes Within the Plate Boundary Zone. *Annu. Rev. Earth Planet. Sci.* 10, 155–190. doi:10.1146/annurev.ea.10.050182.001103

Maestro-González, A., Bárcenas, P., Vázquez, J. T., and Díaz-del-Río, V. (2008). The Role of Basement Inheritance Faults in the Recent Fracture System of the Inner Shelf Around Alboran Island, Western Mediterranean. *Geo-Mar. Lett.* 28, 53–64. doi:10.1007/s00367-007-0089-8

Martinez, F., and Shipboard Scientific Party (2013). R/V Kilo Moana KM1129 [Cruise Data]. doi:10.7284/903698

Martinez, F., and Taylor, B. (1996). Backarc Spreading, Rifting, and Microplate Rotation, Between Transform Faults in the Manus Basin. *Mar. Geophys. Res.* 18, 203–224. doi:10.1007/BF00286078

McKenzie, D. P. (1969). The Relation Between Fault Plane Solutions for Earthquakes and the Directions of the Principal Stresses. *Bull. Seismol. Soc. Am.* 59, 591–601.

Meffre, S., Falloon, T. J., Crawford, T. J., Hoernle, K., Hauff, F., Duncan, R. A., et al. (2012). Basalts Erupted Along the Tongan Fore Arc During Subduction Initiation: Evidence From Geochronology of Dredged Rocks From the Tonga Fore Arc and Trench. *Geochem. Geophys. Geosyst.* 13, Q12003. doi:10.1029/2012GC004335

Merle, S., Chadwick, W., and Rubin, K. (2018). *Processed Gridded Bathymetry Data From the Tonga Volcanic Arc Acquired during R/V Falkor Expedition FK171110 (2017)*. Palisades, NY: Interdisciplinary Earth Data Alliance (IEDA0). doi:10.1594/IEDA/324446

Morley, C. K., Haranya, C., Phoosongsee, W., Pongwapee, S., Kornsawan, A., and Wonganan, N. (2004). Activation of Rift Oblique and Rift Parallel Pre-Existing Fabrics During Extension and Their Effect on Deformation Style: Examples From the Rifts of Thailand. *J. Struct. Geol.* 26, 1803–1829. doi:10.1016/j.jsg.2004.02.014

Moum, T. (2020). Geology and Geochemistry of the Newly-Discovered VOLPA Seafloor Massive Sulfide Deposit, Niua Volcanic Arc Complex, Tonga, SW Pacific. Master's thesis. Toronto (ON): University of Toronto.

Neev, D., Hall, J. K., and Saul, J. M. (1982). The Pelusium Megashear System Across Africa and Associated Lineament Swarms. *J. Geophys. Res.* 87, 1015–1030. doi:10.1029/JB087iB02p01015

Neves, M. C., Searle, R. C., and Bott, M. H. P. (2003). Easter Microplate Dynamics. *J. Geophys. Res.* 108, 2213. doi:10.1029/2001JB000908

Nielsen, S. G., Prytulak, J., Blusztajn, J., Shu, Y., Auro, M., Regelous, M., et al. (2017). Thallium Isotopes as Tracers of Recycled Materials in Subduction Zones: Review and New Data for Lavas From Tonga-Kermadec and Central America. *J. Volcanol. Geotherm. Res.* 339, 23–40. doi:10.1016/j.jvolgeores.2017.04.024

Nijholt, N., and Govers, R. (2015). The Role of Passive Margins on the Evolution of Subduction-Transform Edge Propagators (STEPs). *J. Geophys. Res. Solid Earth* 120, 7203–7230. doi:10.1002/2015JB012202

Nilsson, K., Florendo, F., and Hawkins, J. W. (1989). Petrology of a Nascent Triple Junction, Northeastern Lau Basin. *Eos. Trans. AGU* 70 (73), 1389. doi:10.1029/89EO00329

Park, J.-W., Campbell, I. H., Kim, J., and Moon, J.-W. (2015). The Role of Late Sulfide Saturation in the Formation of a Cu- and Au-Rich Magma: Insights From the Platinum Group Element Geochemistry of Niuatahi-Motutahi Lavas, Tonga Rear Arc. *J. Petrol.* 56, 59–81. doi:10.1093/petrology/egu071

Parson, L., Pearce, J. A., Murton, B., and Hodkinson, R. (1990). Role of ridge Jumps and Ridge Propagation in the Tectonic Evolution of the Lau Back-Arc Basin, Southwest Pacific. *Geology* 18, 470–473. doi:10.1130/0091-7613(1990)018<0470:RORJAR>2.3.CO;2

Pelletier, B., Lagabrielle, Y., Benoit, M., Cabioch, G., Calmant, S., Garel, E., et al. (2001). Newly Identified Segments of the Pacific-Australia Plate Boundary Along the North Fiji Transform Zone. *Earth Planet. Sci. Lett.* 193, 347–358. doi:10.1016/S0012-821X(01)00522-2

Phillips, D. A. (2003). Crustal Motion Studies in the Southwest Pacific: Geodetic Measurements of Plate Convergence in Tonga, Vanuatu and the Solomon Islands. Doctoral dissertation. Honolulu (HI): University of Hawaii at Manoa. Available at: https://search.proquest.com/docview/305327521.

Poreda, R. J., and Craig, H. (1992). He and Sr Isotopes in the Lau Basin Mantle: Depleted and Primitive Mantle Components. *Earth Planet. Sci. Lett.* 113, 487–493. doi:10.1016/0012-821X(92)90126-G

Price, A. A., Jackson, M. G., Blichert-Toft, J., Blusztajn, J., Conatser, C. S., Konter, J. G., et al. (2016). Geochemical Evidence in the Northeast Lau Basin for Subduction of the Cook-Austral Volcanic Chain in the Tonga Trench. *Geochem. Geophys. Geosyst.* 17, 1694–1724. doi:10.1002/2015GC006237

Regelous, M., Turner, S., Falloon, T. J., Taylor, P., Gamble, J., and Green, T. (2008). Mantle Dynamics and Mantle Melting Beneath Niuafo'ou Island and the Northern Lau Back-Arc Basin. *Contrib. Mineral. Petrol.* 156, 103–118. doi:10.1007/s00410-007-0276-7

Resing, J. A., Baker, E. T., Luption, J. E., Lilley, M. D., Rubin, K. H., and Buck, N. J. (2011a). "The Chemistry of Hydrothermal Venting at a Volcano "O", A Large Submarine Volcano in the NE Lau Basin," in Paper Presented at the American Geophysical Union Fall Meeting 2011, San Francisco, CA, December 5–9, 2011. Available at: https://ui.adsabs.harvard.edu/abs/2011AGUFM.V53D2652R/abstract [abstract].

Resing, J. A., Rubin, K. H., Embley, R. W., Lupton, J. E., Baker, E. T., Dziak, R. P., et al. (2011b). Active Submarine Eruption of Boninite in the Northeastern Lau Basin. *Nat. Geosci.* 4, 799–806. doi:10.1038/ngeo1275

Resing, J., and Shipboard Scientific Party (2009). R/V Thomas G. Thompson TN234.

Rubin, K., Embley, R., Arculus, R., and Lupton, J. (2013). "Magmatically Greedy Rear-Arc Volcanoes of the N. Tofua Segment of the Tonga Arc," in Paper Presented at the American Geophysical Union Fall Meeting 2013, San Francisco, CA. Available at: https://ui.adsabs.harvard.edu/abs/2013AGUFM.V13I..04R/abstract [abstract].

Rubin, K., and Embley, R. (2012). Identification and Implications of a Submarine Monogenetic Field in the NE Lau Basin," in Paper Presented at the American Geophysical Union Fall Meeting 2012, San Francisco, CA. Available at: https://ui.adsabs.harvard.edu/abs/2012AGUFM.V44C..08R/abstract [abstract].

Rubin, K. H., and Embley, R. W. (2016). Tectonic and Volcanic Interplays in Earth's Largest and Only Known Active Boninite Volcano Province, in Paper Presented at the Geological Society of America Annual Meeting, Denver, CO, September 25–28, 2016, *GSA Abstracts with Programs* 48 (7). doi:10.1130/abs/2016AM-286764

Rubin, K., and Shipboard Scientific Party (2018). R/V Falkor FK171110 [Cruise Data]. doi:10.7284/907642

Rubin, K., and Shipboard Scientific Party (2010). R/V Kilo Moana KM1024 [Cruise Data]. doi:10.7284/900840

Ruellan, E., Delteil, J., Wright, I., and Matsumoto, T. (2003). From Rifting to Active Spreading in the Lau Basin - Havre Trough Backarc System (SW Pacific): Locking/Unlocking Induced by Seamount Chain Subduction. *Geochem. Geophys. Geosyst.* 4, 8909. doi:10.1029/2001GC000261

Ruellan, E., Huchon, P., Auzende, J.-M., and Gràcia, E. (1994). Propagating Rift and Overlapping Spreading center in the North Fiji Basin. *Mar. Geol.* 116, 37–56. doi:10.1016/0025-3227(94)90167-8

Sandwell, D. T., Müller, R. D., Smith, W. H. F., Garcia, E., and Francis, R. (2014). New global marine gravity model from Cryo-Sat-2 and jason-1 reveals buried tectonic structure. *Science, Vol.* 346, 6205, pp. 65–67. doi:10.1126/science.1258213

Schmid, F., Cremanns, M., Augustin, N., Lange, D., Petersen, F., and Kopp, H. (2021). Microseismicity and Lava Flows Hint at Magmato-Tectonic Processes Near the Southern Tip of the Fonualei Rift and Spreading Center in the Lau Basin. *J. Geophys. Res. Solid Earth* 126, e2020JB021340. doi:10.1029/2020JB021340

Schmid, F., Kopp, H., Schnabel, M., Dannowski, A., Heyde, I., Riedel, M., et al. (2020). Crustal Structure of the Niuafo'ou Microplate and Fonualei Rift and Spreading Center in the Northeastern Lau Basin, Southwestern Pacific. *J. Geophys. Res. Solid Earth* 125, e2019JB019184. doi:10.1029/2019JB019184

Scholz, C. H., and Campos, J. (1995). On the Mechanism of Seismic Decoupling and Back Arc Spreading at Subduction Zones. *J. Geophys. Res.* 100, 22103–22115. doi:10.1029/95JB01869

Schouten, H., Klitgord, K. D., and Gallo, D. G. (1993). Edge-Driven Microplate Kinematics. *J. Geophys. Res.* 98, 6689–6701. doi:10.1029/92JB02749

Sleeper, J. D., Martinez, F., and Arculus, R. (2016). The Fonualei Rift and Spreading Center: Effects of Ultraslow Spreading and Arc Proximity on Back-Arc Crustal Accretion. *J. Geophys. Res. Solid Earth* 121, 4814–4835. doi:10.1002/2016JB013050

Sleeper, J. D., and Martinez, F. (2016). Geology and Kinematics of the Niuafo'ou Microplate in the Northern Lau Basin. *J. Geophys. Res. Solid Earth* 121, 4852–4875. doi:10.1002/2016JB013051

Stewart, M. S., Hannington, M. D., Emberley, J., Baxter, A. T., Krätschell, A., and Petersen, S. (In Press). A new geological map of the Lau Basin reveals crustal growth processes in arc-backarc systems. Geosphere.

Sun, W., Bennett, V. C., Eggins, S. M., Arculus, R. J., and Perfit, M. R. (2003). Rhenium Systematics in Submarine MORB and Back-Arc Basin Glasses: Laser Ablation ICP-MS Results. *Chem. Geol.* 196, 259–281. doi:10.1016/S0009-2541(02)00416-3

Sunkel, G. (1990). Origin of Petrological and Geochemical Variations of Lau basin Lavas (SW Pacific). *Mar. Mining* 9, 205–234.

Tappin, D., Bruns, T., and Geist, E. (1994). "Rifting of the Tonga/Lau ridge and Formation of the Lau Backarc Basin: Evidence from Site 840 on the Tonga Ridge," in Proceedings of the Ocean Drilling Program, Scientific Results. Editors J. Hawkins, L. Parson, and J. Allan (College Station, TX: Ocean Drilling Program), Vol. 135, 367–371.

Taylor, B., and Martinez, F. (2003). Back-Arc Basin Basalt Systematics. *Earth Planet. Sci. Lett.* 210, 481–497. doi:10.1016/0012-1821X(1096)00148-0014310.1016/s0012-821x(03)00167-5

Taylor, B., Zellmer, K., Martinez, F., and Goodliffe, A. (1996). Sea-Floor Spreading in the Lau Back-Arc basin. *Earth Planet. Sci. Lett.* 144, 35–40. doi:10.1016/0012-821X(96)00148-3

Taylor, P. W., and Ewart, A. (1997). "The Tofua Volcanic Arc, Tonga, SW Pacific: Review of Historic Volcanicactivity. Australian Volcanological Investigations (AVI) Occasional Report No. 97/01. (Pymble, New South Wales: Australian Volcanological Investigations).

Tian, L., Castillo, P. R., Hilton, D. R., Hawkins, J. W., Hanan, B. B., and Pietruszka, A. J. (2011). Major and Trace Element and Sr-Nd Isotope Signatures of the Northern Lau Basin Lavas: Implications for the Composition and Dynamics of the Back-Arc Basin Mantle. *J. Geophys. Res.* 116, B11201. doi:10.1029/2011JB008791

Turner, S., Regelous, M., Hawkesworth, C., and Rostami, K. (2006). Partial Melting Processes Above Subducting Plates: Constraints From 231Pa-235U Disequilibria. *Geochim. Cosmochim. Acta* 70, 480–503. doi:10.1016/j.gca.2005.09.004

Uyeda, S., and Kanamori, H. (1979). Back-Arc Opening and the Mode of Subduction. *J. Geophys. Res.* 84, 1049–1061. doi:10.1029/JB084iB03p01049

Volpe, A. M., Douglas Macdougall, J., and Hawkins, J. W. (1988). Lau Basin Basalts (LBB): Trace Element and SrNd Isotopic Evidence for Heterogeneity in Backarc Basin Mantle. *Earth Planet. Sci. Lett.* 90, 174–186. doi:10.1016/0012-821X(88)90099-4

Wang, Z., Park, J.-W., Wang, X., Zou, Z., Kim, J., Zhang, P., et al. (2019). Evolution of Copper Isotopes in Arc Systems: Insights From Lavas and Molten Sulfur in Niuatahi Volcano, Tonga Rear Arc. *Geochim. Cosmochim. Acta* 250, 18–33. doi:10.1016/j.gca.2019.01.040

Wright, T. J., Sigmundsson, F., Pagli, C., Belachew, M., Hamling, I. J., Brandsdóttir, B., et al. (2012). Geophysical Constraints on the Dynamics of Spreading Centres from Rifting Episodes on Land. *Nat. Geosci.* 5, 242–250. doi:10.1038/ngeo1428

Wysoczanski, R., Leonard, G., Gill, J., Wright, I., Calvert, A., McIntosh, W., et al. (2019). Ar-Ar Age Constraints on the Timing of Havre Trough Opening and Magmatism. *New Zealand J. Geol. Geophys.* 62, 371–377. doi:10.1080/00288306.2019.1602059

Zellmer, K. E., and Taylor, B. (2001). A Three-Plate Kinematic Model for Lau Basin Opening. *Geochem. Geophys. Geosyst.* 2, 2000GC000106. doi:10.1029/2000GC000106

Zhang, H., Yan, Q., Li, C., Zhu, Z., Zhao, R., and Shi, X. (2018). Geochemistry of Diverse Lava Types From the Lau Basin (South West Pacific): Implications for Complex Back-Arc Mantle Dynamics. *Geol. J.* 54, 3643–3659. doi:10.1002/gj.3354

Zhu, H., Du, L., Li, X., Zhang, Z., and Sun, W. (2020). Calcium Isotopic Fractionation during Plate Subduction: Constraints From Back-Arc Basin Basalts. *Geochim. Cosmochim. Acta* 270, 379–393. doi:10.1016/j.gca.2019.12.004

Conflict of Interest: The authors declare that the research was conducted in the absence of any commercial or financial relationships that could be construed as a potential conflict of interest.